ICFO-INSTITUT DE CIÈNCIES FOTÒNIQUES

&

UPC-UNIVERSITAT POLITÈCNICA DE CATALUNYA

Micro-nano structured optical devices using $Ge_2Sb_2Te_5$

MIQUEL RUDÉ

Thesis Advisor: Prof. Valerio Pruneri

PhD Thesis - 2016

Abstract

Photonic devices are key to implement future communication and information technologies. Their success is largely determined by our capability to appropriately control light in such devices, especially in future reconfigurable networks. Light does not interact with itself, thus one usually needs the use of an active material. Phase change materials are a potential candidate to implement this functionality. These materials are a group of chemical compounds that exist in more than one stable phase, each with largely different electrical and optical properties. Moreover, they can be rapidly and reversibly switched between these phases using electrical or optical pulses.

This thesis is devoted to the design and implementation of micro-nano structured photonic devices incorporating the phase-change material $Ge_2Sb_2Te_5$ (GST). The thesis first investigates how to fabricate thin films of different phase-change materials in a repeatable manner and characterizes their main properties, especially those of GST. This includes an investigation of their composition, the conditions required to reversibly switch between the amorphous and crystalline phases, as well as their optical properties in each of the stable phases. Three different applications are then demonstrated, each of them based on a different functionality.

The first application is an optical switch operating at telecommunication wavelengths. The device is implemented using a racetrack resonator partially covered with GST. The transmission resonances present in this system are controlled using an infrared laser that triggers phase transitions in the GST layer, thus modifying the shape and position of the resonance wavelength between two states. The switch has an on/off ratio of ~ 12

dB and response times of ~ 5 μs.

In the second application, control of surface plasmon polaritons in Au waveguides is demonstrated. This is achieved using a cladding layer of GST. 100 % modulation is achieved for large GST areas and thermal crystallization, while up to 30 % modulation is achieved using small GST areas and laser crystallization.

The third application is related to nanohole arrays covered with GST thin films. The effect of phase transitions in the transmission resonances of these structures is investigated for three geometries. Wavelengths shifts as large as 385 nm are demonstrated in devices with broad resonances. Additionally, excitation of GST with short pulses allows for ultrafast tuning of these resonances in the ps regime without the need for a phase transition. Finally, tuning of narrow resonances with shifts of 13 nm is also shown.

In summary, the studies and applications contained in this thesis demonstrate the potential of GST and, in general, phase-change materials, to address optical tunability, which is an essential function in a wide range of optical devices.

Resum

Els dispositius fotònics són un dels principals candidats per implementar les futures tecnologies de la informació i de la comunicació. El seu èxit dependrà en gran mesura de la capacitat de controlar la llum en aquests dispositius, en particular en dispositius reprogramables. Degut a que la llum no interactua amb ella mateixa normalment es necessita usar un material actiu per assolir aquest control. Els materials de canvi de fase són un dels possibles candidats per implementar aquesta funcionalitat. Aquest conjunt de compostos químics es caracteritzen per tenir més d'una fase estable. Cada una d'aquestes fases presenta unes propietats òptiques i elèctriques molt diferents. A més a més els canvis de fase en aquests materials es poden realitzar molt ràpidament i de manera reversible mitjançant polsos elèctrics o òptics.

Aquesta tesis descriu el disseny i l'implementació de nous dispositius òptics micro i nanoestructurats usant el material de canvi de fase $Ge_2Sb_2Te_5$ (GST). A la primera part de la tesis s'investiga com fabricar capes primes de diferents materials de canvi de fase de manera repetible i es caracteritzen les seves propietats principals, en especial les del GST. Això inclou una investigació de la seva composició, les condicions necessàries per induir reversiblement transicions de fase entre els estats amorf i cristal·lí, així com mesures de les propietats òptiques de cada una de les fases. Aquests resultats es faran servir per implementar després tres aplicacions, cada una de les quals té una funció diferent.

La primera aplicació és un interruptor òptic que traballa a una longitud d'ona de 1550 nm. El dispositiu està implementat en un anell resonador parcialment recobert amb una capa prima de GST. Les ressonàncies en

transmissió d'aquest sistema són controlades amb un làser infraroig que indueix transicions de fase en la capa de GST, modificant la forma i posició de la ressonància entre dos estats. L'interruptor té una relació entre els estats 'on' i 'off' de 12 dB i un temps de resposta d'uns 5 μs.

En la segona aplicació es demostra el control de plasmons de superfície propagant-se a través d'una guia d'ona d'or. Això s'aconsegueix fent servir una capa de GST dipositada sobre el dispositiu. Usant grans àrees de GST i cristal·lització per temperatura es poden aconseguir modulacions del 100 %, mentre que usant petites àrees de GST i cristal·lització làser es demostren modulacions de fins el 30 %.

La tercera aplicació explora la combinació d'estructures periòdiques de nanoforats amb capes de GST. En aquest experiment s'investiga l'efecte de les transicions de fase en les ressonàncies de transmissió usant tres geomteries diferents. En dispositius amb ressonàncies amples es poden desplaçaments en la longitud d'ona d'aquestes ressonàncies de 385 nm. A més a més, excitant la capa de GST amb polsos curts es mesuren canvis d'aquestes ressonàncies en una escala de temps de ps sense la necessitat d'induir una transició de fase. Per últim també es demostren desplaçments en la longitud d'ona de fins a 13 nm en dispositius amb ressonàncies estretes.

Els estudis i aplicacions descrits en aquesta tesi demostren el potencial del GST i dels materials de canvi de fase en general per implementar dispositius òptics sintonitzables, que realitzaran una funció essencial en futures tecnologies basades en la llum.

Acknowledgments

I would like to express my gratitude to several people, without whom this thesis would not have been possible.

First of all, I would like to thank Prof. Valerio Pruneri for giving me the opportunity to work in the Optoelectronics group at ICFO, and for his continous support, help, and ideas during the course of this thesis.

Also, I would like to thank Prof. Robert Simpson for introducing me to the amazing field of PCMs, and for his support during the early stages of my PhD, as well as to Dr. Jan Renger, Dr. Josselin Pello, Dr. Timothy Miller, Vahagn Mkhitaryan and Prof. Romain Quidant, Prof. Simon Wall, and Prof. Javier García de Abajo, for fruitful collaborations and discussions that led to the work presented here. It has been a pleasure working with all of them. A special mention also to all the researchers, technicians, and staff who helped me during my stay at ICFO, and to Lisa Ruby, for carefully proofreading this manuscript.

Personally, I would like to thank all the OPTO members and ICFO colleagues for making my daily work much more pleasant. And also to all the ICFO friends, music lovers, and 'afterwork' mates, with whom I have shared many special and funny moments. It has been an amazing experience.

Finally, I am also indebted to my family for all his support, especially my brother, my parents, and my grandmother. This thesis is dedicated to them.

Contents

Abstract **i**

Resum **iii**

Acknowledgments **v**

List of Figures **xi**

List of Tables **xiii**

List of Publications **xv**

1 Introduction **1**
1.1 Phase-change materials overview 2
1.1.1 Ge-Te-Sb ternary system 2
1.1.2 Structural properties of PCMs 3
1.1.3 Phase transitions 4
1.1.4 GST 6
1.2 Phase-change materials for photonics 8
1.3 Aims of the thesis 10
1.4 Thesis outline 11

2 Fabrication and characterization of PCMs **13**
2.1 PCMs growth 13
2.1.1 Sputtering deposition 13

2.1.2 GeTe-Sb_2Te_3 co-sputtering 14
2.2 GST characterization 18
2.3 Si_3N_4 fabrication and characterization 19

3 Optical Switching in Silicon Racetrack Resonators 23
3.1 Ring resonators 24
3.2 Experimental realization 26
3.2.1 Device fabrication 28
3.2.2 Experimental set-up 29
3.2.3 Crystallization/reamorphization parameters . . . 32
3.2.4 Temperature calibration 33
3.3 Experimental results 35
3.3.1 Static measurements 35
3.3.2 Time response of the RR 37
3.4 Conclusions 39

4 Active Control of Surface Plasmon Polaritons with GST 41
4.1 Surface plasmon polaritons at planar interfaces 42
4.2 Design and simulation of plasmonic waveguides with GST 44
4.2.1 Influence of the PMMA layer 47
4.2.2 Influence of the SiO_2 layer 48
4.3 Propagation length and contrast of the SPP waveguides . 49
4.3.1 Device fabrication and experimental set-up . . . 50
4.3.2 Experimental results 50
4.4 Nonvolatile plasmonic switch 51
4.5 Conclusions 57

5 Ultrafast and broadband tuning of resonant optical nanostructures 59
5.1 Au NH array with GST inside the holes 60
5.1.1 Device fabrication 60
5.1.2 Transmission measurements 61
5.1.3 Ultrafast response of the NH array 62
5.2 Au NH array without GST in the holes 65
5.3 Au NH array in a Si_3N_4 membrane 67

5.4 Physical origin of the change in the transmission spectrum 68
5.5 Conclusions 70

6 Conclusions and Outlook 73

Bibliography 77

List of Figures

1.1 Ternary phase diagram of Ge, Sb and Te 2
1.2 Schematic diagram of phase transitions in PCMs 4
1.3 Typical temperature profiles during crystallization and reamorphization of a PCM 5

2.1 Deposition rates of GeTe and Sb_2Te_3 15
2.2 EDX spectra of PCM compounds 17
2.3 Transmission of GST thin films as a function of thickness 18
2.4 Contrast in the transmitted intensity for different GST films 19
2.5 Transmission spectra of the fabricated Si_xN_y films 21

3.1 Schematic of a RR 24
3.2 Microscope image of the RR optical switch 27
3.3 Schematic of the optical switch set-up 30
3.4 Spectrum of the RR 31
3.5 Switching cycle in GST 33
3.6 Temperature effects in the RR 34
3.7 Evolution of the spectrum during one cycle 36
3.8 Time response of the RR 38

4.1 SPP propagation at a planar interface 42
4.2 Cross section of the simulated SPP waveguides 44
4.3 Normalized intensity profile of the eigenmodes in the SPP waveguide structure 46

4.4 Decay lenght of the SPP_{Au} mode as a function of PMMA thickness 47
4.5 Propagation constants of the eigenmodes as a function of SiO_2 thickness 48
4.6 Schematic of the GST covered SPP waveguide 49
4.7 Intensity image of the SPP waveguides 51
4.8 Normalized intensity of the SPP as a function of L_G . . . 52
4.9 Schematic of the nonvolatile plasmonic swith 53
4.10 Optical microscope image of the nonvolatile plasmonic switch 54
4.11 Intensity images of the transmitted light at λ = 1550 nm . 55
4.12 Contrast of the SPP waveguides as a function of GST width 57

5.1 Schematic of a NH array with GST inside the holes . . . 61
5.2 Experimental and simulated transmission spectra of the NH array with GST inside the holes 62
5.3 Simulated electric field distribution on- and off- resonance 63
5.4 Time response of the NH array during the initial 3 ps . . 64
5.5 Experimental and simulated transmission spectra of the NH array without GST in the holes 65
5.6 Evolution of the NH array spectrum for an electrically triggered phase transition 66
5.7 Schematic of a NH array on a Si_3N_4 membrane. 67
5.8 Normalized transmission of the NH array suspended on a Si_3N_4 membrane 68

List of Tables

1.1 Applications of PCMs in photonic devices 9

2.1 Conditions for GeTe and Sb_2Te_3 plasma 'striking' . . . 15
2.2 Sputtering conditions of PCM compounds 16
2.3 Measured atomic percentages of PCM compounds 17
2.4 Sputtering test for Si_3N_4 20

3.1 GST and Si_3N_4 sputtering conditions 28
3.2 Values of the thermo-optic effect in the RR 35
3.3 Evolution of the RR parameters during one cycle 37

4.1 Values of the dielectric function used to simulate the SPP waveguides 45
4.2 Propagation constants of the eigenmodes in the SPP waveguides 46

List of Publications

Publications included in this thesis

A M. Rudé, J. Pello, R. E. Simpson, J. Osmond, G. Roelkens, J. J. van der Tol, and V. Pruneri, "Optical switching at 1.55 μm in silicon racetrack resonators using phase change materials," *Appl. Phys. Lett.*, vol. 103, no. 14, p. 141119, 2013.

B M. Rudé, R. E. Simpson, R. Quidant, V. Pruneri, and J. Renger, "Active control of surface plasmon waveguides with a phase change material," *ACS Photonics*, vol. 2, no. 6, pp. 669–674, 2015.

C L. Waldecker, T. A. Miller, M. Rudé, R. Bertoni, J. Osmond, V. Pruneri, R. E. Simpson, R. Ernstorfer, and S. Wall, "Time-domain separation of optical properties from structural transitions in resonantly bonded materials," *Nature Mater.*, vol. 14, no. 10, pp. 991–995, 2015.

D M. Rudé, V. Mkhitaryan, A. E. Cetin, T. A. Miller, A. Carrilero, S. Wall, F. J. G. de Abajo, H. Altug, and V. Pruneri, "Ultrafast and broadband tuning of resonant optical nanostructures using phase-change materials," *Adv. Opt. Mater.*, 2016.

Other relevant publications and conference contributions

E T. A. Miller, M. Rudé, V. Pruneri, and S. Wall, "Ultrafast optical response of the amorphous and crystalline states of the phase change material $Ge_2Sb_2Te_5$," *Phys. Rev. B*, vol. 94, p. 024301, Jul 2016.

F V. Mkhitaryan, D. S. Ghosh, M. Rudé, J. Canet- Ferrer, R. Abraham Maniyara, K. K. Gopalan, and V. Pruneri, "Tunable complete optical absorption in multilayer structures including $Ge_2Sb_2Te_5$ without lithographic patterns," Accepted in *Adv. Opt. Mater.*

G J. Pello, J. J. G. M. van der Tol, M. K. Smit, M. Rudé, R. E. Simpson, V. Pruneri, S. Keyvaninia, and G. Roelkens, "Chalcogenides applied to microring switching," *ECIO - European conference on Integrated Optics*, Barcelona (Spain), 2012.

H R. E. Simpson, J. Renger, M. Rudé, R. Quidant, and V. Pruneri, "Active plasmonics based on phase change materials," *ECIO - European Conference on Integrated Optics*, Barcelona (Spain), 2012.

I M. Rudé, J. Pello, R. E. Simpson, J. J. G. M. van der Tol, and V. Pruneri, "Optical switch based on miroring resonators and phase change materials," *CLEO EUROPE/IQEC*, Germany, 2013.

J L. Waldecker, T. A. Miller, M. Rudé, V. Pruneri, R. E. Simpson, R. Ernstorfer, S. Wall, "Competition between thermal and non-thermal processes during femtosecond switching of phase change materials," *UP - International Conference on Ultrafast Phenomena*, Japan, 2014.

K M. Rudé, R. E. Simpson, R. Quidant, V. Pruneri, and J. Renger, "Controlling surface plasmon polariton propagation using phase change materials" *CLEO EUROPE/IQEC*, Germany, 2015.

Chapter 1

Introduction

Phase-change materials (PCMs) are a group of chemical compounds characterized by having an amorphous and a crystalline structural phase, with each phase exhibiting largely different optical and electrical properties. Moreover they have the ability to rapidly and reversibly switch between these phases a large number of times under the application of an appropriate thermal cycle, which can be provided by means of electrical or optical pulses [1]. The discovery of these materials dates back to 1968, when Ovshinsky [2] demonstrated a huge change in the electrical resistivity of thin films containing Te, As, Si and Ge, upon phase transitions triggered by the application of an external voltage. This particular feature soon made PCMs a strong candidate to store digital information by encoding bits into different phases of the material. Over the next decades research on PCMs led to the discovery of a large number of new compounds and their application in optical storage media [3, 4](CDs, DVDs and BluRay Disks) and non-volatile flash memories [5, 6](PCRAM).

These features, in particular the high contrast in the optical properties, which are not found in other photonic materials, make PCMs attractive candidates to control and manipulate light. The main aim of this thesis is the development of novel photonic devices using PCMs.

1.1 Phase-change materials overview

1.1.1 Ge-Te-Sb ternary system

Among all PCMs known nowadays, the prototypical compounds are those of the Ge-Te-Sb ternary system [7]. Figure 1.1 shows the ternary phase diagram, together with the most significant PCM classes.

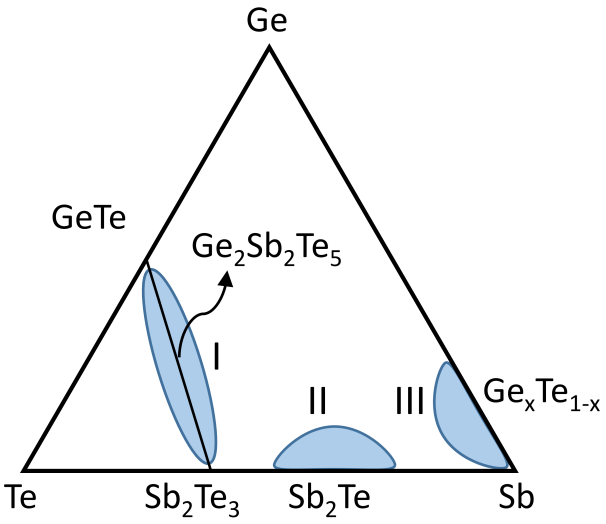

Figure 1.1: Ternary phase diagram of Ge, Sb and Te.

In this diagram the GeTe - Sb_2Te_3 tie-line (I), the area around Sb_2Te (II) and the region around Sb (Ge_xSb_{1-x}) (III) are the three main classes of PCMs. PCMs in regions I and II have been used in CD-RW, DVD-RW, and the first and second generation of DVD-RAM, as well as single and dual layer Blu-Ray disks [3]. This ternary system, in particular the Sb_2Te_3 tie-line, has been extensively studied. Among the compounds of the tie-line, $Ge_2Sb_2Te_5$ (GST) is the most used, mainly due to its superior performance in terms of stability, phase transition speed and optical contrast [1, 8].

1.1.2 Structural properties of PCMs

The amorphous phase of a PCM is a disordered structure consisting of a network of covalently bonded atoms. As any amorphous material, this phase is metastable, having higher entropy than the lowest energy crystalline state. It also lacks the long-range translational and rotational symmetry characteristic of a crystal. Yet, the atomic arrangement is not completely random, and is mainly manifested in the form of short-range order (SRO), consisting of nearest-neighbor atomic correlations in the 2 - 4 Å length scale. This glassy phase behaves like a dielectric with large resistivity and low absorption.

On the other hand, the crystalline phase is an ordered material of resonantly bonded atoms, and in contrast to the amorphous phase, exhibits long-range order (LRO). Resonant bonding is the fingerprint of PCMs. This type of chemical bond, called resonant bonding by Linus Pauling [9], is present in certain crystalline materials, in which half-filled p-bands form two bonds that are aligned over second and higher neighbors [10, 11]. These bonds, in which electrons are highly delocalized, are responsible for the high optical constants of the crystalline state in the low-energy region of the spectra [12]. Due to the lack of LRO, they cannot be present in the amorphous phase, whose bonds are formed by electron pairs instead.

The crystalline phase of PCMs in the tie-line is a metastable, distorted rocksalt structure. In the case of GST, Te atoms form one sublattice while Ge atoms, Sb atoms and vacancies randomly form the other sublattice [3, 13–15]. It is also important to mention that although both the amorphous and the crystalline phases have SRO, the local structure of each phase is different [16]. In the amorphous phase the coordination numbers follow the 8 - N rule, while the coordination numbers of the crystalline phase are higher than expected from this rule. This difference of LRO is also a particular feature of PCMs and is not found in conventional covalent semiconductors, where the local structure in the amorphous and crystalline phases is the same, and therefore does not exhibit such a large optical contrast. This change in both the bonding and the local order is

believed to be responsible for the large optical contrast of PCMs [10, 17].

1.1.3 Phase transitions

The phase transition diagram for PCMs is schematically depicted in Figure 1.2.

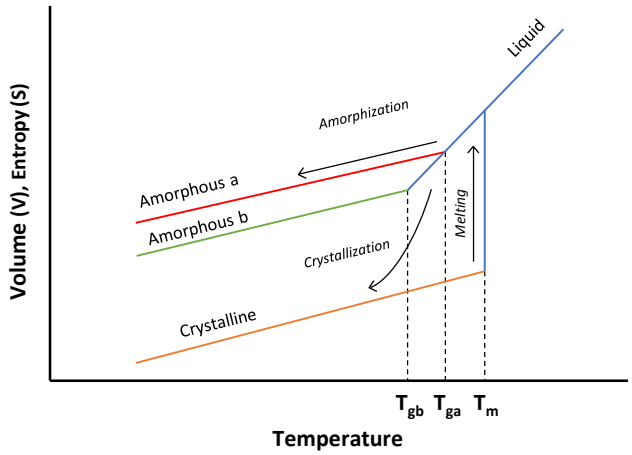

Figure 1.2: Schematic diagram of phase transitions in PCMs.

Starting from the liquid phase, which is achieved for $T > T_m$, cooling can either crystallize a PCM via a first-order phase transition near T_m, or the material can be supercooled below T_m and transformed into a glass state near the glass transition temperature T_g. The final amorphous state will depend on the cooling rate. Glass a in Figure 1.2 will be obtained using high cooling rates, while glass b will be obtained for lower cooling rates. Moreover, a higher cooling rate shifts T_g to higher temperatures ($T_{ga} > T_{gb}$).

Thus, the cooling rate will determine the final state of the material. If this rate is smaller than the kinetics of the crystallization process, the material will transform into the lower free energy crystalline phase, ac-

companied by a sharp change in volume and entropy. Otherwise, for high cooling rates the PCM will become quenched into the amorphous phase in a narrow temperature range near T_g. Once this amorphous phase is cooled below T_g the system is no longer able to rearrange itself into a crystalline structure. Contrary to the crystalline phase, the amorphous phase does not undergo any sharp change in volume and will be in a metastable state with a volume and entropy that will depend on the cooling rate.

In practical applications, these phase transitions are triggered using either optical or electrical pulses. The amorphous to crystalline transition is achieved by applying low-power, long pulses, in order to increase the temperature of the amorphous phase between T_g and T_m, as illustrated in Figure 1.3. The polycrystalline structure obtained will depend on the temperature profile applied to the material. Moreover, as crystallization of PCMs is an activated process following an Arrhenius behaviour, the crystallization temperature increases with the heating rate [18].

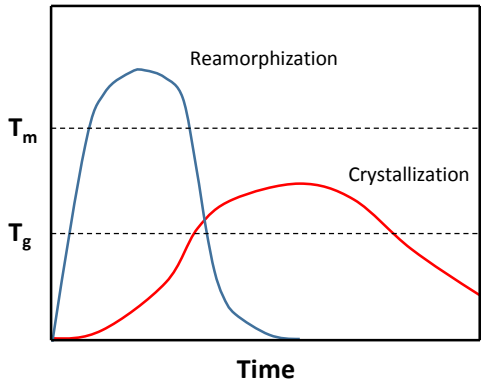

Figure 1.3: Typical temperature profiles during crystallization (red) and reamorphization (blue) of a PCM.

On the other hand, in order to reamorphize a crystalline area one needs

to melt the material and then cool it down fast enough to quench the liquid into the amorphous phase. This can be achieved using high-power, short-pulses and a proper thermal design in order to rapidly extract the generated heat.

It is also important to note that PCMs on the ternary diagram can crystallize in two different ways. Compounds in region I are called nucleation-dominated materials, while those in region II follow a growth-dominated crystallization mechanism [1, 19]. GST belongs to the first class of compounds. Crystallization of GST starts with the appearance of small nuclei in the initial amorphous film, and is followed by their growth over a small distance, until the crystallites touch each other. This process determines the crystallization rate and usually takes place in tens of nanoseconds. Several factors can influence this growing rate, especially film thickness [20, 21].

1.1.4 GST

GST is the prototypical PCM in the tie-line. Apart from the amorphous and the distorted cubic (fcc) phases, GST has a third, high-temperature stable hexagonal phase, which has even larger optical constants and conductivity. Although this phase is not used for practical applications it is still interesting from a physical point of view. The main electrical and optical properties of each of these phases are explained below. Most of the given values, including mobility, optical constants, and bandgap, are just orientative and are generally affected by many parameters. These include preparation conditions, stoichiometry, and the thermal cycle used to trigger the phase transition, to mention a few.

Hexagonal GST

The hexagonal phase of GST is a narrow-gap degenerate semiconductor with a bandgap of $E_g \sim 0.5$ eV. This phase is p-type and has a hole concentration of around $n_h \sim 3{\cdot}10^{20}$ cm^{-3} and a mobility of $\mu \sim 30$ cm^2/(V·s) at room temperature (RT) [22,23]. This behavior is consistent with the ex-

istence of Ge/Sb vacancies in the lattice structure [24]. The conductivity of this phase increases with decreasing temperature, mainly due to lower phonon scattering at low temperatures which increases the mobility.

The refractive index of hexagonal GST increases from $n \sim 1$ in the UV region up to $n \sim 8$ at 2 eV, and then stays nearly constant in the IR region of the spectra [22, 25]. The behaviour of the absorption coefficient is different. It initially increases from $k \sim 2$ at 5 eV to $k \sim 5$ at 2 eV and then suddenly decreases to $k \sim 0$ for energies below 1 eV. As a result of the high carrier concentration at RT, its value increases again at low energies (< 0.4 eV) due to free-carrier absorption [26, 27].

Fcc GST

The fcc phase is a p-type degenerate semiconductor with the same bandgap as the hexagonal phase ($E_g \sim 0.5$ eV). It has a hole concentration of $n_h \sim 10^{20}$ cm^{-3} and a mobility of $\mu \sim 1$ cm^2/(V·s) at RT [22, 23]. These values are smaller than those of the hexagonal phase. However, contrary to the hexagonal phase, the conductivity of the fcc phase increases with temperature due to an increase of the carrier concentration and a small increase of the mobility.

The optical properties of this phase are quite similar to the hexagonal phase. The refractive index follows the same general trend over the whole spectra, remaining always slightly smaller, and reaching a maximum value of $n \sim 7.5$ at 2 eV. Then it stays nearly constant at a value of $n \sim 6$ in the IR region. The values of the absorption are also similar and slightly lower over the whole spectra, with a maximum of $k \sim 4.5$ at 2 eV. This phase also has free carrier absorption for low energies (< 0.4 eV).

Amorphous GST

The amorphous phase is also p-type but has a larger bandgap of E_g = 0.7 eV. Attempts at measuring the transport properties still show significant ambiguities due to experimental and theoretical difficulties in determining these values in amorphous materials [28–32]. In any event the resistivity

is at least 2-3 orders of magnitude higher than the fcc phase, with typical values of $\rho \sim 280\ \Omega{\cdot}\text{cm}^{-1}$ [29]. The conductivity of the amorphous phase increases exponentially with temperature due to the excitation of charge carriers.

The refractive index of the amorphous phase is larger than that of the crystalline phases in the 2-5 eV range, but remains smaller for energies below 2 eV. Its value increases from $n \sim 2$ at 5 eV to a maximum of $n \sim 5$ at 5 eV and then decreases again to $n \sim 4$ and stays constant in the whole IR region. The absorption coefficient is always smaller than that of the crystalline phases. It reaches a maximum of $k \sim 2.5$ at 3 eV and then decreases to $k = 0$ at 1 eV. This phase does not have free-carrier absorption and the absorption coefficient remains $k = 0$ in the IR region.

1.2 Phase-change materials for photonics

The high contrast in the optical and electrical properties, the stability of the amorphous phase and the fast transition times are the main properties that led to the application of PCMs in optical and electrical memories. A few years ago researchers realized that these features could also make PCMs attractive candidates for other applications in photonics, and research into this field has been growing since then, with several devices already demonstrated. Overall, two main lines of research can be distinguished. The first is the use of PCMs in integrated photonic devices. This is a promising approach to implement non-volatile devices, in which the state of the device is stored without the need for any external stimulus. Several devices have been demonstrated, including optical switches [33] and photonic memories [34]. Also interesting is the possibility of using PCMs to perform neuromorphic computing [35,36] and multi-level memories [37]. In another, more recent, direction, the combination of PCMs in multilayer structures has also led to proposals [38–40] and demonstrations of tunable perfect absorbers [41, 42] in different regions of the spectrum, as well as tunable nanoantennas arrays [43, 44], and tunable multicolor coatings [45,46]. Table 1.1 describes in detail some of these applications.

Reference	*Application*
Cao et al. [47]	Broadband perfect absorber in the IR combining GST with Au squares. 10 % tuning of the absorbance after phase-transitions. Polarization independent.
Cao et al. [39]	Broadband perfect absorber in the visible combining GST with Au squares. Wide-angle incidence up to 80^{o} and polarization independent.
Dong et al. [41]	Perfect absorber in the visible combining GST with Al nanogratings. Polarization-dependent.
Hira et al. [43]	Switching of localized surface plasmon resonances on Au nanoparticles using a GST thin film.
Hosseini et al. [48]	Display and data visualization using ultrathin GST layers. Electrically controlled color changes in GST pixels of nanoscale size. Flexible displays also demonstrated.
Michel et al. [49]	Tuning of Al nanoantenna resonances in the mid-IR. Maximum resonance shifts of $\sim$ 20 %
Ríos et al. [37]	Non-volatile and multi-level (up to 8 bits) all-photonic memory using a GST thin film placed on top of a Si waveguide. Single shot optical readout with speeds close to 1 GHz.
Schlich et al. [46]	Color switching in thin films of GST induced with fs laser pulses.
Tanaka et al. [33]	Optical switch in a multi-mode Si waveguide with a cladding layer of GST. Laser triggered phase transitions and 12.6 dB extinction ratio.
Tittl et al. [42]	Switchable plasmonic perfect absorber in the mid-IR using Al nanoantenna arrays. Strong reflection contrasts ($\sim$ 60 %) and resonance wavelengths shifts ($\sim$ 25 %) upon phase transitions.
Wright et al. [35]	Optically controlled phase-change processor capable of performing the four basic arithmetic functions. Demonstration of biologically inspired computations with a phase-change memflector (optical analogue of a memristor).

Table 1.1: Applications of PCMs in photonic devices

1.3 Aims of the thesis

This thesis is devoted to the development of novel photonic devices that exploit the particular features of GST to implement new functionalities. In particular, the main aims of the thesis are the following:

- Fabrication of thin films of PCMs on the Sb_2Te_3-GeTe tie-line with a specified composition, in particular GST. Investigation of the optical properties of these films for different thicknesses both in the amorphous and crystalline phases of the material. Additionally, fabrication and optical characterization of Si_3N_4 films to be used as heat-management and protective layers.

- Design, fabrication and experimental demonstration of non-volatile, optically controlled switches using GST as the active material, in which the two states of the switch are encoded in the two stable phases of the material. Two different devices, which rely on the same principle of operation, are investigated:

  - An optical switch implemented on a Si racetrack resonator covered with GST. In this device the phase of the GST changes the position and shape of the resonances present in this system between two well defined states.

  - A plasmonic switch, where the propagation of surface plasmons polaritons (SPPs) along Au/SiO_2 waveguide is inihibited by the transition of a GST film between the amorphous and crystalline phases.

- Demonstration of tunability in nanohole (NH) arrays on thin Au films using a GST layer. Phase transitions allow one to modify the resonances in these systems, obtaining large wavelength shifts and amplitude modulations.

1.4 Thesis outline

The outline of the thesis is as follows:

Chapter 2 describes the fabrication and characterization of PCM compounds on the Sb_2Te_3-GeTe tie-line. This includes finding the appropriate parameters to deposit each composition in the sputtering, calibration of the deposition rates, and an analysis of their composition using EDX. The optical properties of GST films of different thicknesses for each phase are also investigated. In addition, this chapter describes the conditions necessary to deposit Si_3N_4 films by reactive sputtering using N_2, and measurements of the optical properties of these films.

Chapter 3 introduces a non-volatile optical switch working at telecomm. wavelengths. The switch is based on a Si racetrack resonator containing a GST thin film on top, whose phase is controlled using an IR laser. Part of these results were used for Publication A.

Chapter 4 describes the design and implementation of a non-volatile plasmonic switch on a Au waveguide covered with a GST area. The chapter also includes simulation of the device and experimental measurements of different geometries of the GST layer. The results presented in this chapter were published in Publication B.

Chapter 5 introduces three different devices that combine GST thin films with nanohole arrays patterned on Au. The transmission spectra for each phase of GST is simulated and measured for each different device, and an analytical model for nanohole arrays with GST is also introduced, obtaining results that qualitatively agree with the experimental measurements. These results were published as part of Publications C and D. Finally, Chapter 6 summarizes the main results of this thesis and gives a brief outlook for future improvements.

Chapter 2

Fabrication and characterization of PCMs

This chapter introduces the techniques developed to grow PCM films with compositions on the GeTe-Sb_2Te_3 pseudobinary system, in particular GST, as well as their characterization. These results will be used to realize the devices presented in the next chapters. The fabrication and characterization of Si_3N_4 films, which will be used in some of the devices to protect and improve heat confinement in GST films, is also introduced.

2.1 PCMs growth

2.1.1 Sputtering deposition

PCMs were grown using the sputtering deposition method, a Physical Vapor Deposition (PVD) technique that allows one to deposit virtually any kind of material [50]. The basic operation of sputtering consists of introducing a process gas (Ar in this case) into a vacuum chamber. Then an electric field is applied between the target, which contains the material to be sputtered, and the substrate. This electric field ionizes the Ar gas, creating a plasma of Ar^+ ions. These positive charges are accelerated towards the target placed at the bottom of the chamber and collide with the

target, detaching particles, which are then deposited on the substrate. The quality and properties of the films obtained by this method is, thus, governed by a great variety of parameters, including deposition rate, pressure of the process gas, initial vacuum level, and substrate material and temperature, to name a few. These parameters need to be adjusted to obtain films with the desired properties.

PCM compounds were deposited using the ATC Orion 8 HV sputtering system, manufactured by AJA International Inc. [51]. The ATC Orion 8 HV is a computer-controlled RF/DC deposition system with 2 RF and 2 DC power sources, which allows co-sputtering from different targets. The diameter of the targets is 2 inches and up to 7 targets can be installed inside the vacuum chamber. The substrates are placed on a rotating sample holder that can spin at a maximum frequency of 40 revolutions/min. The main chamber is connected to a turbo pump that allows a vacuum level of 5×10^{-8} Torr to be reached. Additionally, O_2 and N_2 gas lines are available as process gases that can be mixed with Ar in order to obtain nitrides and oxides by reactive sputtering.

2.1.2 GeTe-Sb_2Te_3 co-sputtering

The deposition of PCM compounds in the GeTe-Sb_2Te_3 was done by RF co-sputtering from two stoichiometric targets (99.999 % purity) of GeTe and Sb_2Te_3. The first step was to find the appropriate parameters to deposit films of GeTe and Sb_2Te_3 with a certain thickness. In order to deposit any material by sputtering, one first needs to create a plasma of Ar^+ ions confined around the target. The shutter of the target remains closed during this part of the process, to avoid deposition of material on the substrate. This first part of the process is called 'striking', and usually requires higher pressures and/or powers than those used in the deposition process. The striking conditions were found by fixing the Ar flow to 10 sccm and iteratively increasing the pressure and power. These values are given in Table 2.1.

Once the striking conditions had been found, the next step was to calibrate the deposition rate of the films. This was achieved by fixing the

Target	Ar flow (sccm)	Strike pressure (mTorr)	Strike power (W)
GeTe	10	40	45
Sb_2Te_3	10	40	45

Table 2.1: Conditions for GeTe and Sb_2Te_3 plasma 'striking'.

Ar flow at 10 sccm, the process pressure at 3.75 mTorr, and changing the RF power applied to the target. For each power, the sputtering time was fixed at 1800 s to obtain a thick film, whose thickness was then measured in a profilometer in order to obtain the deposition rate. Figure 2.1 shows the deposition rate as a function of the RF power for GeTe and Sb_2Te_3.

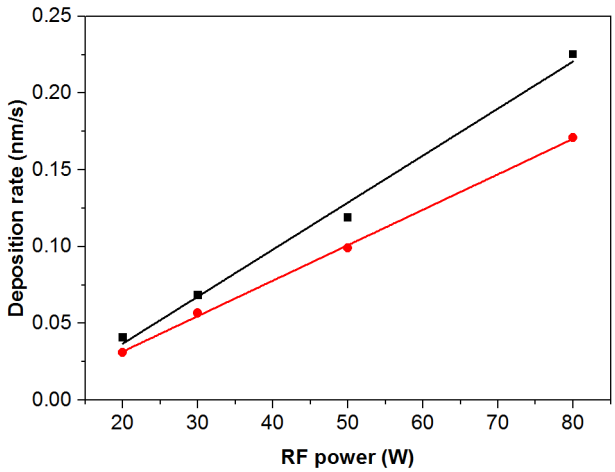

Figure 2.1: Deposition rates of GeTe and Sb_2Te_3 as a function of the applied RF power.

By co-sputtering GeTe and Sb_2Te_3 one can obtain the compounds in the pseudobinary tie-line according to the following chemical reaction:

$$x\text{GeTe} + y\text{Sb}_2\text{Te}_3 \rightarrow \text{Ge}_x\text{Sb}_{2x}\text{Te}_{x+3y} \tag{2.1}$$

Thus, for instance, $Ge_2Sb_2Te_5$ can be obtained with x = 2 and y = 1. In order to find out the appropriate parameters to deposit a certain composition, one needs to obtain the relation between the deposition rates (d_{GeTe}, $d_{Sb_2Te_3}$) and x and y. The number of molecules (n_i; i = GeTe, Sb_2Te_3) deposited per unit time and unit area is $n_i = d_i\rho_i/a_i$, where ρ_i and a_i are the densities and molar masses, respectively. Using this and relation 2.1, the relation between deposition rates is:

$$\frac{d_{GeTe}}{d_{Sb_2Te_3}} = \frac{\rho_{Sb_2Te_3} a_{GeTe}}{\rho_{GeTe} a_{Sb_2Te_3}} \frac{x}{y} \tag{2.2}$$

By fixing $d_{Sb_2Te_3}$ one can calculate the RF power required to deposit a certain compound using Eq. 2.2 and Figure 2.1. This was done for three different compositions, as shown in Table 2.2.

PCM	x/y	$P_{Sb_2Te_3}$(W)	P_{GeTe}(W)	$d_{Sb_2Te_3}$(nm/s)	d_{GeTe}(nm/s)
$Ge_2Sb_2Te_5$	2	50	44.73	0.13	0.09
$GeSb_4Te_7$	0.5	70	20.47	0.19	0.03
$Ge_8Sb_2Te_{11}$	8	20	50.56	0.03	0.10

Table 2.2: Sputtering conditions of PCM compounds.

Test samples of each composition were then co-sputtered for 1800 s on Si substrates using the RF powers calculated above. The composition of the films was obtained using an EDX system placed inside an SEM (FEI - Inspect F). This system allows one to extract the atomic percentages with an accuracy of $\approx$ 5 %. The comparison between the measured atomic percentages and the stoichiometric ones, as well as the EDX spectra, are shown in Table 2.3 and Figure 2.2, respectively.

The measurements confirmed that the obtained atomic percentages are close to those of the stoichiometric compounds. Thus, PCMs on the GeTe-Sb_2Te_3 pseudobinary system can be deposited using co-sputtering with the RF powers found above, while their thicknesses can be controlled just by changing the sputtering time.

PCM	Theory			EDX		
	Ge %	Sb %	Te %	Ge %	Sb %	Te %
$Ge_2Sb_2Te_5$	22.2	22.2	55.6	22.7	20.7	56.6
$GeSb_4Te_7$	8.3	33.3	58.4	6.8	34.3	58.9
$Ge_8Sb_2Te_{11}$	38.1	9.5	52.4	42.1	9.6	48.3

Table 2.3: Measured atomic percentages of PCM compounds.

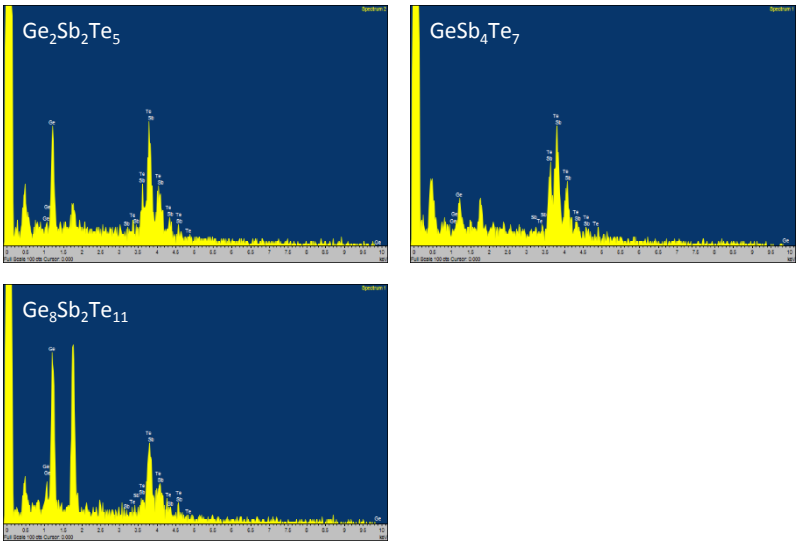

Figure 2.2: EDX spectra of PCM compounds.

2.2 GST characterization

Among PCM compounds in the tie-line, $Ge_2Sb_2Te_5$ (GST) is both the most studied and the most used composition. This is mainly due to its long-term stability at room temperature, fast crystallization times and large contrast in the optical properties upon a phase transition [4]. This composition will be used to perform the experiments presented in this thesis.

Once the parameters needed to deposit GST were found, the next step was to characterize its properties. The deposition rate of GST with the parameters given in Table 2.2 was found to be d_{GST} = 0.22 nm/s from profilometry measurements. Thin films of different thicknesses were grown on fused SiO_2 substrates at room temperature, ensuring that the as-deposited GST films were in the amorphous state. The transmission of these films, both in the visible and near infrared (NIR), was then measured in a spectrophotometer (Lambda 950, PerkinElmer). Crystallization of the films was achieved by heating them on a hot plate at 200 °C for 1 h. After this thermal treatment, the transmission decreased due to the increase in the refractive index and absorption coefficient, thus confirming that the films had crystallized, and that the as-deposited films were in the amorphous phase. These measurements are shown in Figure 2.3.

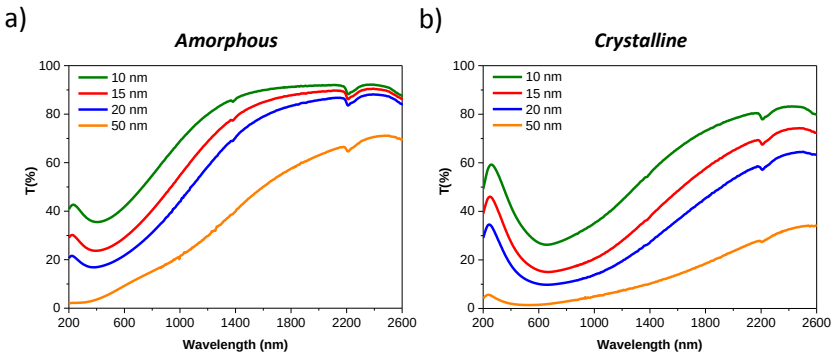

Figure 2.3: Transmission of GST thin films as a function of thickness.

The transmission at a fixed wavelength decreases exponentially with the thickness, as expected from the Beer-Lambert law. For a fixed thickness, the overall transmission decreases after crystallization, due to the increased optical constants, except in the short wavelength regime, where crystalline GST is more transparent. The contrast between phases can be calculated from these measurements and is given in Figure 2.4.

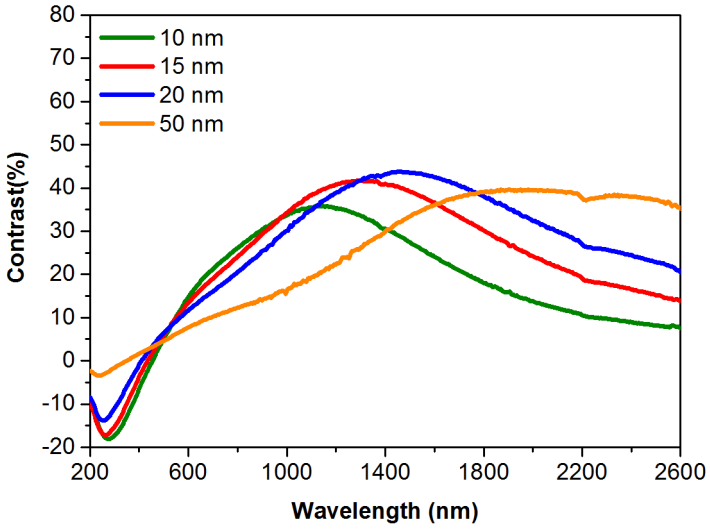

Figure 2.4: Contrast in the transmitted intensity for different GST films.

The contrast achieves values up to 50 %. For 20 nm films, which will be used in most of the experiments, this maximum contrast occurs close to λ = 1550 nm, which is important for optical devices using GST that work at telecommunication wavelengths.

2.3 Si_3N_4 fabrication and characterization

The fabrication of Si_3N_4 films was achieved by reactive sputtering. DC sputtering from a Si target is combined with a mixture of N_2 and Ar as

process gases. Si and N_2 react inside the chamber, and thin films with a composition of the form Si_xN_y are deposited on the substrate. The stoichiometry of the composition depends on the relative proportions of Si and N_2 during the sputtering process. The parameters needed to obtain Si_3N_4 were found by fixing the DC power on the Si target to 40 W and changing the amount of N_2 entering into the chamber. The total pressure and flow of gases was always fixed at 3.75 mTorr and 10 sccm, respectively. Table 2.4 summarizes the parameters used for each test as well as the thicknesses and deposition rates of each sample.

Sample	1	2	3	4	5
P_{Si} (W)	40	40	40	40	40
Ar flow (sccm)	10	9	8	7	5
N_2 flow (sccm)	0	1	2	3	5
Time (s)	1800	1800	1800	1800	1800
Thickness (nm)	40.1	34.6	33.9	31.2	24.8
d (nm/s)	0.0222	0.0192	0.0188	0.0173	00138

Table 2.4: Sputtering test for Si_3N_4.

In order to obtain Si_3N_4 one needs enough N_2 inside the chamber. The minimum amount of N_2 required was found by measuring the transmission of the fabricated films, as shown in Figure 2.5.

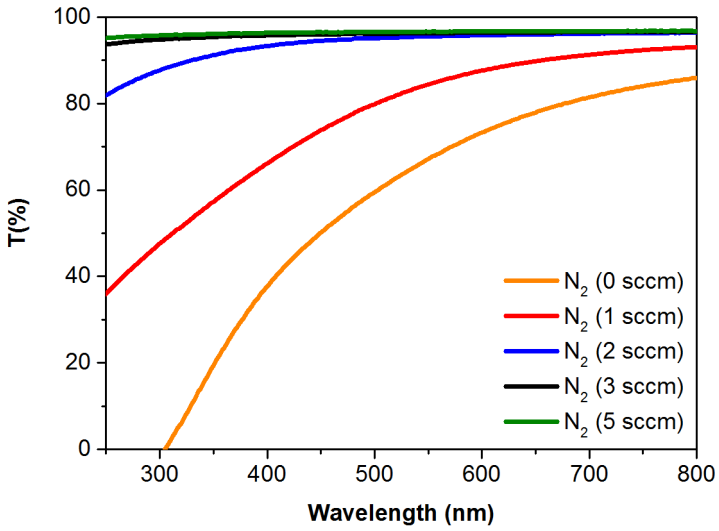

Figure 2.5: Transmission spectra of the fabricated Si_xN_y films.

From Figure **??** one can see that the transparency increases with the amount of N_2 present during the process, and it saturates for values of $N_2 > 3$ sccm, indicating that there is enough N_2 to deposit Si_3N_4. A flow of N_2 of 3 sccm was used to deposit subsequent Si_3N_4 films. The transmission of pure Si, which corresponds to the case with 0 sccm of N_2, is also shown as a reference.

Chapter 3

Optical Switching in Silicon Racetrack Resonators

The development of photonic devices that can process optical signals in a reliable and low-cost manner is a key step towards future optical technologies. Due to its high refractive index and the compatibility with current CMOS fabrication technologies, silicon (Si) based devices are one of the main candidates to implement such applications, and several devices, including modulators [52–56], filters [57] and wavelength division multiplexers (WDM) [58] have already been demonstrated. One of the key requirements of these technologies will also be the ability to program reconfigurable optical circuits that can retain their state without any continuous external source, which would allow implementing applications as diverse as photonic routers or non-von Neumann computing.

This chapter introduces a non-volatile Si racetrack resonator (RR) optical switch. The switch is based on the use of a GST thin film placed on top of the RR, which, upon transition from its amorphous to its crystalline phase and the accompanying change in its optical properties, modifies the losses and effective refractive index of the optical mode inside the RR. This allows light propagating along an adjacent waveguide to be transmitted when GST is in the crystalline phase (“on” state), while confining it inside the RR when GST is in the amorphous phase (“off” state).

3.1 Ring resonators

A ring resonator consists of an optical waveguide bent to form a closed loop [59]. Whenever the optical path length of the ring is an integer multiple of the wavelength, a resonance occurs and light is trapped inside it. For this to happen there must be some mechanism to couple light in and out of the ring. This is usually accomplished via evanescent wave coupling from a bus waveguide adjacent to it. Then, the transmission spectra of the bus waveguide will show a series of dips corresponding to ring resonances. The ring resonators used in this work are called "racetrack" resonators (RR) because the coupling region contains a small straight waveguide in parallel with the bus waveguide to improve the coupling efficiency. A schematic of such a RR is shown in Figure 3.1.

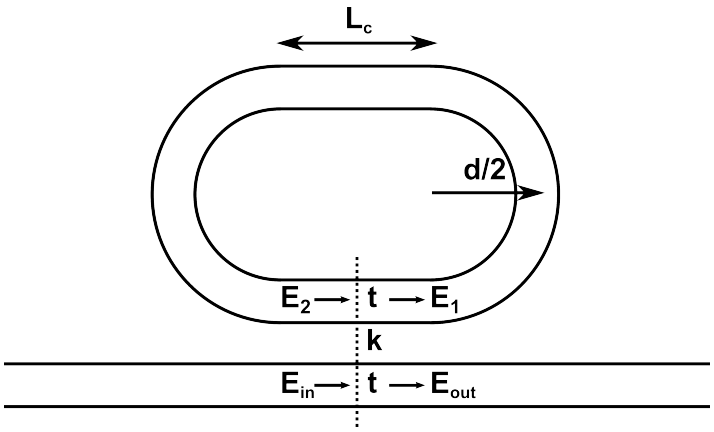

Figure 3.1: Schematic of a RR and the adjacent bus waveguide.

The spectral properties of the RR can be calculated by assuming continuous wave (CW) operation and matching the fields in the coupling region. Assuming there are no reflections back to the waveguide the fields in the coupling region are related by the following expressions:

$$E_1 = irE_{in} + tE_2 \tag{3.1}$$
$$E_2 = \tau E_1 e^{i\phi} \tag{3.2}$$
$$E_{out} = tE_{in} + irE_2 \tag{3.3}$$

where t and r are the self- and cross-coupling coefficients, respectively, that define the amplitude splitting ratios in the coupler. Assuming there are no losses in the coupling region these parameters satisfy the relation $t^2 + r^2 = 1$. The phase shift after one round trip is given by $\phi = \frac{2\pi}{\lambda} n_{eff} L$, where $L = \pi d + 2L_c$ is the length of the RR, and τ is the electric field attenuation due to losses inside the RR. These include propagation losses, losses due to mismatches between the straight and the circular regions of the RR, as well as light scattering caused by roughness at the vertical sidewalls. Combining Eq. 3.1, 3.2 and 3.3 one obtains the ratio between the transmitted and the incident field:

$$\frac{E_{out}}{E_{in}} = \frac{t - \tau e^{i\phi}}{1 - t\tau e^{i\phi}} \tag{3.4}$$

and the intensity transmission, obtained by squaring Eq. 3.4, is given by:

$$\frac{I_{out}}{I_{in}} = \frac{t^2 - 2t\tau\cos\phi + \tau^2}{1 - 2t\tau\cos\phi + t^2\tau^2} \tag{3.5}$$

When the phase ϕ is an integer multiple of 2π the ring is on resonance and the corresponding resonance wavelength is:

$$\lambda_{res} = \frac{n_{eff} L}{m}, \quad m \in \mathbb{Z} \tag{3.6}$$

For each resonance one can calculate the corresponding quality factor by dividing λ_{res} by the full width at half maximum (FWHM):

$$Q = \frac{\lambda_{res}}{FWHM} \tag{3.7}$$

Eq. 3.5, 3.6 and 3.7 define the main properties of a RR. By measuring the transmission spectrum of a real device one can directly calculate λ_{res} and Q. Fitting the measrued transmission to Eq. 3.5 one obtains the values of t, r, τ and n_{eff}, which will be used later in this chapter to see the influence of a phase transition in a GST layer placed on top of the RR.

3.2 Experimental realization

The optical switch is implemented using a Si RR with an overcladding layer of the PCM GST. At telecommunication wavelengths GST exhibits high contrast in its optical properties upon transitions between the covalently bonded amorphous phase and the resonantly bonded crystalline phase [17, 60]($n_{\text{cryst}} - n_{\text{amorph}} = 2.5$; $k_{\text{cryst}} - k_{\text{amorph}} = 1$ at 1.55 μm) [1] and these transitions can be used to modify the resonant frequency and the losses of the RR. Figure 3.2 shows an optical microscope image of the actual device.

The RR has a bend radius of 5 μm and a coupling region of 3 μm. Another RR with the same dimensions but without the GST layer is used as a reference during the measurements. Both the RR and the bus waveguides have a cross section of 220×440 nm^2, designed to support only a single mode at λ = 1.55 μm. The RR and the bus waveguides are separated by a 200 nm gap in the coupling region. Moreover the bus waveguide has grating couplers at both ends [61], which are used to deliver light into the device and monitor the transmitted spectrum using single mode fibers (SMF). A GST layer with an area of 3×5 μm^2 and a thickness of 20 nm is placed on top of the first RR and separated from it by a 50 nm buffer layer of SiO_2. This buffer layer is used to control the overlap of the evanescent field of the RR with the GST film. The GST area is covered with a 20 nm Si_3N_4 film used to prevent oxidation and achieve good thermal isolation, which is critical to achieve laser triggered phase transitions.

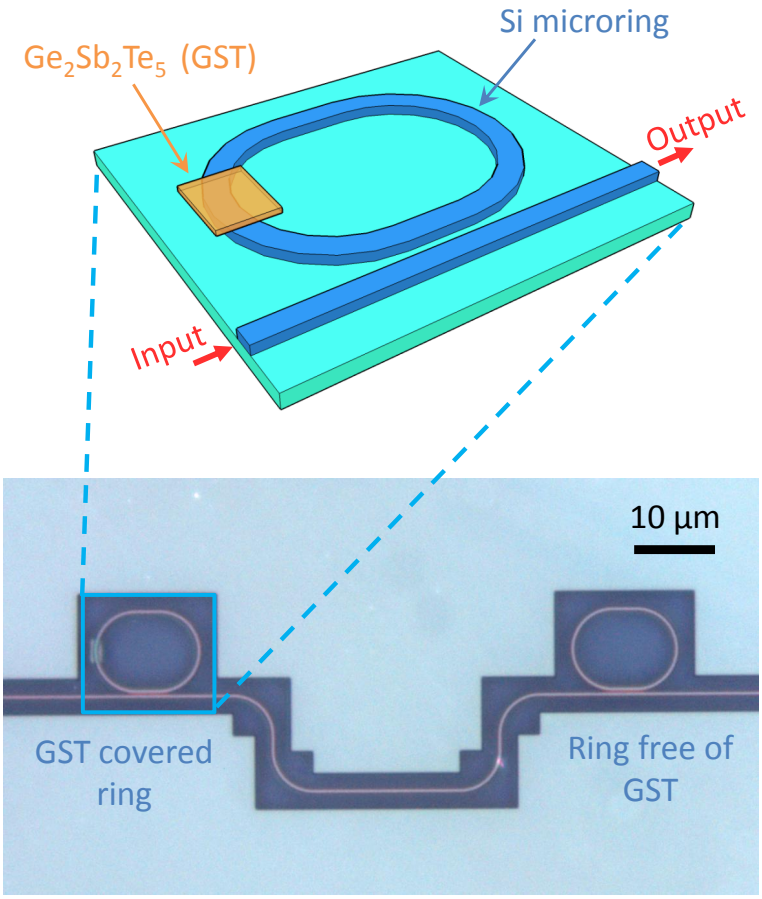

Figure 3.2: Optical microscope image of the two RRs coupled to a bus waveguide. The first of them (left) contains the overcladding layer of GST.

3.2.1 Device fabrication

The RR, waveguides and grating couplers were designed at Ghent University and fabricated at IMEC (Belgium). The devices were fabricated on top of a silicon-on-insulator (SOI) substrate with 2 μm of buried oxide using 248 nm deep UV lithography, following a previously developed process [62]. The buffer layer (50 nm) of SiO_2 was deposited on top of the Si waveguide using plasma-enhanced chemical vapor deposition (PECVD). Subsequently, polymethylmethracylate resist (PMMA) was spun on the SOI die and the area where the GST was to be deposited was opened using e-beam lithography. A 20 nm thick GST film was deposited on this area using radio frequency (RF) sputtering from two stoichiometric targets of GeTe and Sb_2Te_3. X-ray diffraction from other GST films, which were prepared under the same conditions, confirmed the structural phase of the film to be amorphous. The 20 nm film of Si_3N_4 was grown on top of the GST by reactively DC sputtering Si using a mixture of Ar and N_2 as the process gases. The sputtering conditions for these films are summarized in Table 3.1. The sample was then put in an acetone bath for 30 minutes to remove the PMMA and lift off the excess material. Finally, the device was rinsed with isopropanol and blow-dried.

	$Ge_2Sb_2Te_5$		Si_3N_4	
Targets	GeTe	Sb_2Te_3	Si	
Power (type)	50 W (RF)	45 W (RF)	40 W (DC)	
Process gases	Ar		Ar	N_2
Gas flow	10 sccm		7 sccm	3 sccm
Gas pressure	3.75 mTorr		3.75 mTorr	
Time	90 s		1200 s	
Temperature	298 K		298 K	

Table 3.1: Sputtering conditions for the GST and Si_3N_4 films. The sputtering targets in all cases are 3" in diameter.

3.2.2 Experimental set-up

The optical set-up used to perform the experiment is shown in Figure 3.3. Phase transitions in the GST layer were triggered by heating a 1 μm spot with a pulsed laser diode (LD) at λ = 975 nm. The electrical current driving the laser was maintained at a sub-threshold level during the experiment. Electrical pulses with tunable length and amplitude were generated in a function generator (Agilent 33220A, 20 MHz) and amplified by a high-gain amplifier (MiniCircuits LZY-22+, 43 dB gain) before being sent to the LD through a bias-T circuit. The output optical pulses were coupled into a SMF, collimated and focused down to a diameter of 1 μm on the sample using a 0.6 NA (50x) objective. Homogeneous illumination of the sample was achieved using a white LED and an aspheric condenser lens that sent white light to the sample using a pellicle mirror (PM), while cross-polarizers were used to optimize the contrast of the image. Both the illumination and the laser beams travelled back along the optical path and were focused onto a CCD camera using a 75 mm focal length lens. An additional short-pass infrared filter (IF) (λ_{cutoff} = 950 nm) was added before this lens in order to attenuate the laser beam and avoid damage to the camera. Precise alignment of the laser spot with the GST was achieved by monitoring the reflected laser spot and the sample image with the camera and using a 3-axis stepper motorized stage to control the sample position and the focus of the 975 nm laser radiation.

Two SMFs were used to couple light from a broadband (λ_{min} = 1520 nm to λ_{max} = 1580 nm) amplified spontaneous emission (ASE) source. The transmitted spectrum was recorded with an optical spectrum analyzer (OSA). Both fibers were cleaved and mounted on holders to ensure 10° incidence with the grating and achieve maximum coupling efficiency [61]. Optimal coupling to and from the waveguide was achieved using two 3-axis micro-positioners. The device temperature was controlled by placing the sample on top of a thermo electrical cooler (TEC).

Figure 3.4 shows the full transmission spectrum of the device shown in Figure 3.2 with the GST set in its amorphous phase. Since the device contains two RRs in series, the dips in the figure appear grouped in pairs.

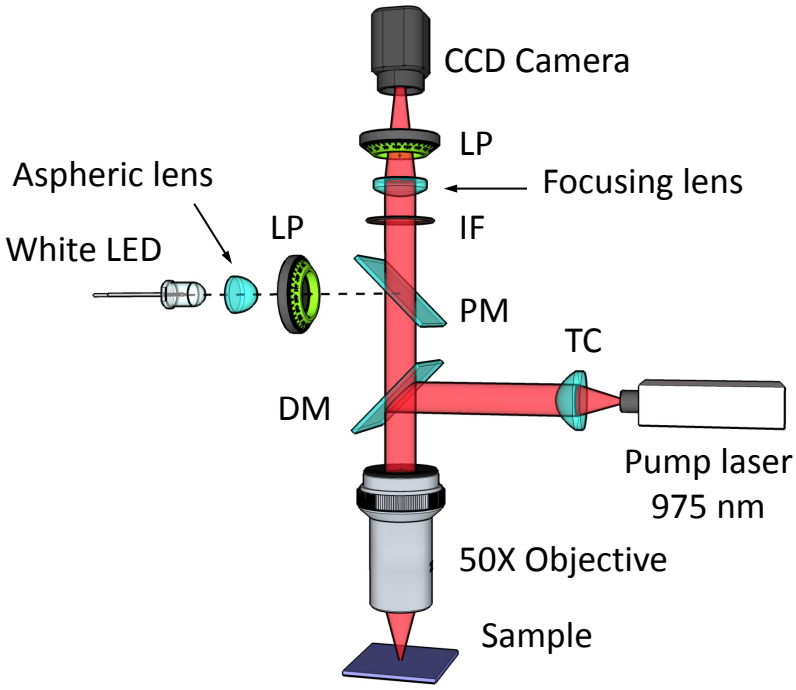

Figure 3.3: Schematic of the experimental set-up (LP: Linear polarizer, DM: Dichroic mirror, IF: Infrared filter, PM: Pellicle mirror, TC: Triplet collimator).

The left one in each pair corresponds to the RR with GST and is modified upon phase transitions, while the right one, corresponding to the bare RR, is used as a reference. Although the amorphous phase of GST has a small extinction coefficient ($k_{\text{amorph}} = 0.1$ at $\lambda = 1.55$ μm) [1], its presence increases the losses in the resonator, an effect which can be seen by measuring the Q factors of the bare RR ($Q = 6528$), and the RR covered with amorphous GST ($Q = 5656$).

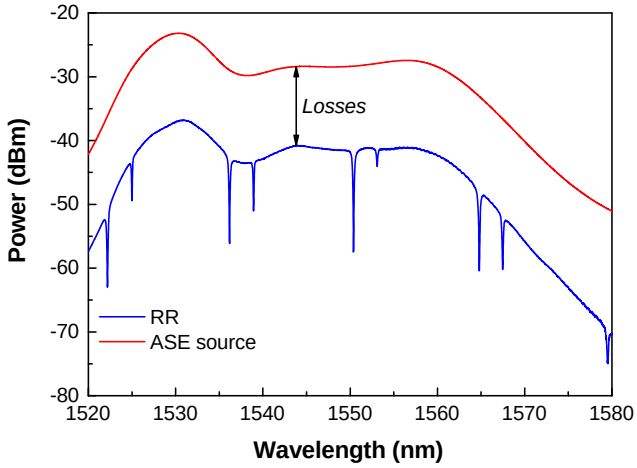

Figure 3.4: Transmission spectrum of the RR between 1520 and 1580 nm. Note that the spectrum is not flat due to the ASE source. The spectrum of the ASE source is also shown as a reference.

For wavelengths outside the resonant condition, the difference between the two spectra in Figure 3.4 allows one to estimate the total losses in the device (P_{loss}), including both coupling losses at the input/output gratings (ξ_c), and propagation losses in the waveguide (ξ_{wg}). These are related by $P_{\text{loss}}(\text{dB}) = 2\xi_c + L_{wg}\xi_{wg}$, where L_{wg} is the waveguide length (L_{wg} = 0.35 cm). Waveguide losses are estimated to be $\xi_{wg} \approx 9.5$ dB/cm for this particular kind of waveguide [62], and are approximately constant in the wavelength range of the experiment. In general, ξ_c is also

wavelength dependent and so is P_{loss}. In this case P_{loss}, calculated from the values in Figure 3.4, varies between a minimum of 12.4 dB at λ = 1545 nm, where the grating is designed to have maximum efficiency, to a maximum value of 24 dB around λ = 1580 nm. Thus the minimum coupling losses are estimated to be ξ_c = 4.5 dB per grating at λ = 1545 nm, close to the telecommunication wavelength where the optical switch is implemented.

3.2.3 Crystallization/reamorphization parameters

Before starting the measurements in the RR it was first necessary to find the parameters (pulse power and duration) needed to crystallize and reamorphize the GST layer, as these are strongly dependent on the composition, thickness and the thermal properties of the surrounding environment [63, 64]. To this end a test sample with the same structure (50 nm SiO_2/20 nm GST/20 nm Si_3N_4) was fabricated on top of a SOI substrate. The switching parameters were then found by iteratively increasing the laser pulse duration and power. Crystalline marks in the as-deposited film (amorphous state), which appear as a brighter area in the optical microscope due to the higher refractive index (see Figure 3.5), were repeatedly created with low power (12 mW) long pulses (t_p^c = 300 ns, t_r^c = 80 ns), while reamorphization of a crystalline area was achieved with high power (45 mW) short pulses (t_p^a = 20 ns, t_r^a = 8 ns), where t_p^i and t_r^i denote the pulse FWHM and rising/falling times, respectively. The whole crystallization/reamorphization process is shown in Figure 3.5.

As the diameter of the created spots was approximately the same as the laser beam (1 μm), the laser repetition rate (f_r = 50 kHz) in this test was chosen to be synchronized with the motor velocity such that there was approximatley 1 pulse/μm, thus creating a continuous line of crystalline/amorphous material. It is also interesting to estimate the temperatures required to achieve each of the phase transitions in this particular set-up. For low heating rates, crystallization of GST can be achieved by heating it above the glass transition temperature (T_g = 428 K), and then slowly cooling the material to let the atoms rearrange themselves into a

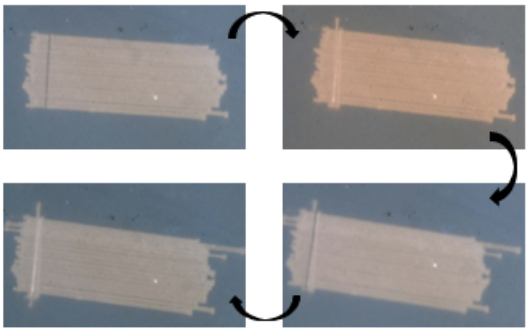

Figure 3.5: Optical microscope images of two crystallization/reamorphization cycles. A line of reamorphized GST is created on an initially crystalline area by scanning the laser across the sample with the motorized stage (top left). This process is then repeated with crystallization pulses (top right), recovering the initial crystalline state. Cyclability of GST is shown by applying the same cycle a second time, obtaining the same results (bottom right and bottom left).

crystalline structure. However, crystallization of GST is an activated process following an Arrhenius behavior, and thus the crystallization temperature increases with heating rate [18]. In this case (t_r^c = 80 ns) the heating rate is on the order of 10^7 K·s^{-1} and we expect crystallization temperatures $T_c > 625$ K. On the other hand to reamorphize crystalline GST one only needs enough temperature to melt the GST layer (T_m = 888 K) and sufficiently large cooling rates ($\sim 10^8$-10^9 K·s^{-1}) to quench it, which can be achieved using fast falling times (t_r^a = 8 ns).

3.2.4 Temperature calibration

The final step before proceeding with the actual measurements was to analyze the effect of temperature on the transmission spectrum. Si RRs are known to be quite sensitive to external variations in temperature, mainly due to the thermo-optic effect in Si [65, 66]. An increase of just 1 °C (which increases n_{eff} proportionally) can manifest as a non-negligible redshift in the resonant wavelength. In order to check this effect in our

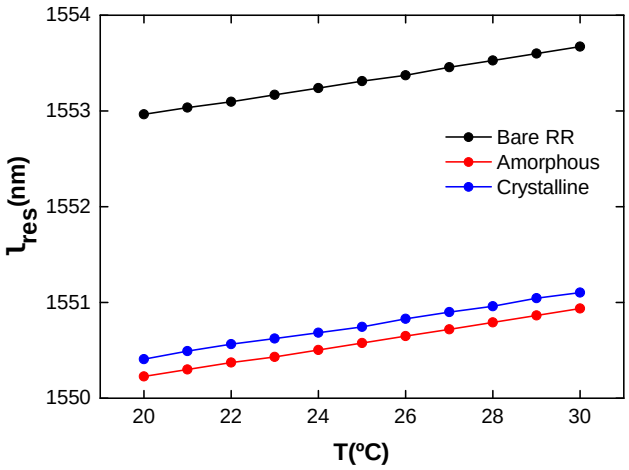

Figure 3.6: Evolution of the resonance wavelength as a function of temperature in a bare RR (black), a RR with amorphous GST (red) and a RR with crystalline GST (blue).

devices, we scanned the temperature from 20° to 30° using the TEC. This was done both in the bare RR and the RR with GST in each of the phases. The dependence of the resonance wavelength on temperature for each case is shown in Figure 3.6.

The value of λ_{res} depends on the effective refractive index and the length of the RR, both of which can change as a function of temperature. This change is given by:

$$\frac{d\lambda_{res}}{dT} = \frac{1}{m}\left(\frac{dn_{eff}}{dT}L + n_{eff}\frac{dL}{dT}\right) \tag{3.8}$$

$$= \frac{L}{m}\left(\alpha_t + n_{eff}\beta_t\right) \tag{3.9}$$

Here α_t is the "effective" thermo-optic coefficient and β_t = 2.6·10^{-6} K^{-1} [67] is the thermal expansion coefficient of Si. For small tempera-

ture variations n_{eff} and L can be assumed to behave linearly with temperature, thus α_t and β_t are constant and $d\lambda_{res}/dT$ corresponds to the slope of the curves in Figure 3.6. Assuming that $n_{eff}\beta_t \ll \alpha_t$ ($n_{eff}\beta_t \approx 6.04{\cdot}10^{-6}$ K^{-1} for the bare RR), Eq. 3.9 reduces to:

$$\alpha_t = \frac{n_{eff}}{\lambda_{res}} \frac{d\lambda_{res}}{dT} \tag{3.10}$$

Where we used $m/L = n_{eff}/\lambda_{res}$. This equation allows one to calculate α_t. Table 3.2 summarizes the values of these parameters for each case (λ_{res} and n_{eff} are measured at 22 °C).

	λ_{res}(nm)	$d\lambda_{res}/dT$ (pm·K^{-1})	n_{eff}	α_t (K^{-1})
Bare RR	1553.096	70.8	2.3245	$1.0597{\cdot}10^{-4}$
GST_{am}	1550.384	70.8	2.3204	$1.0597{\cdot}10^{-4}$
GST_{crys}	1550.552	69.6	2.3207	$1.0417{\cdot}10^{-4}$

Table 3.2: Values of the "effective" thermo-optic coefficient calculated using the slope of the curves in Figure 3.6 for a bare RR and a RR with amorphous and crystalline GST.

Note that from the table, one can confirm that $n_{eff}\beta_t \ll \alpha_t$ and that the effect of the phase transition on the value of α_t is also negligible. The value of the shifts (≈ 70-71 pm·K^{-1}) is in agreement with previous studies on similar devices [68, 69]. As it will be seen later, this shift is comparable to the increase in λ_{res} upon crystallization of the GST film. Therefore, in order to evaluate only the effect due to the GST phase transition the temperature during the experiment was fixed at 22 ± 0.02 °C.

3.3 Experimental results

3.3.1 Static measurements

Static measurements were performed starting with the as-deposited amorphous GST film. Using the IR laser at λ = 975 nm, crystallization pulses

with the parameters found in the test sample were used to crystallize the GST film. As the GST area (3x1.5 μm^2) was larger than the focused laser spot (1 μm), it was necessary to move the laser in steps of 1 μm across this area and repeatedly apply crystallization pulses until all the GST film was crystallized. This could be achieved with just 3 shots along the axis waveguide (Figure 3.7(a)). The same process was repeated using reamorphization pulses to recover the transmissivity at λ = 1.55 μm, thus completing a full cycle (Figure 3.7(b)).

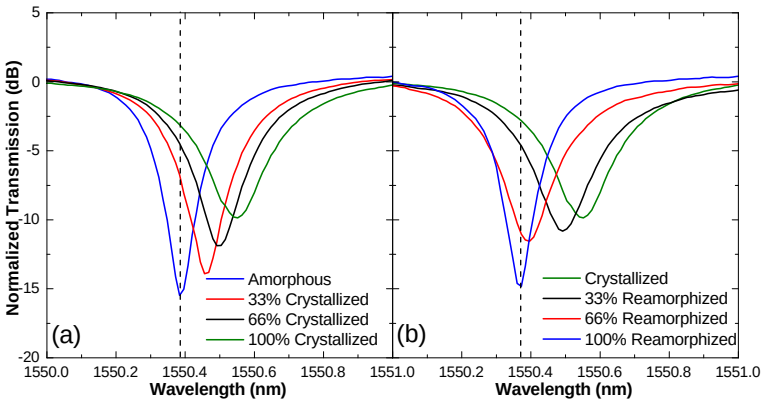

Figure 3.7: Evolution of the transmission spectrum during crystallization (a) and reamorphization (b) of the 1.5x3 μm^2 GST area.

By fitting the data in Figure 3.7 to Eq. 3.5, it was possible to determine the evolution of the main parameters defining the resonance during one crystallization/reamorphization cycle. These are shown in Table 3.3 ($\alpha = -2\log\tau/L$ are the losses in cm^{-1} after one round trip).

One can see that the optical properties of the final amorphous state are quite similar to those of the initial one, with maximum differences in the values lying around 5% , indicating that the switch performance is robust and reversible. These small differences can be explained due to the out-of-equilibrium nature of the sputter deposition process, as it is known that the optical properties of the as-deposited amorphous state and the laser reamorphized state can be slightly different. Indeed, it is normally

State	λ_{res}(nm)	n_{eff}	τ	t	Q	α(cm^{-1})
Amorphous	1550.384	2.3204	0.986	0.983	5656	7.570
33% Cryst.	1550.456	2.3205	0.977	0.983	4433	12.326
66% Cryst.	1550.492	2.3206	0.974	0.983	4115	13.983
Crystallized	1550.552	2.3207	0.968	0.983	3641	16.841
33% Ream.	1550.492	2.3206	0.972	0.983	3922	15.145
66% Ream.	1550.396	2.3205	0.974	0.983	4051	14.454
Reamorphized	1550.372	2.3204	0.986	0.983	5411	7.160

Table 3.3: Evolution of the RR parameters during the crystallization/reamorphization cycle.

necessary to cycle GST data storage devices more than 100 times before the electrical properties of the amorphous state converge to a stable value [70]. Table 3.3 also shows a clear effect of the amorphous to crystalline phase transition on the transmission. The increase in the refractive index of GST upon crystallization increases the averaged-out effective refractive index of the ring by 0.0003, producing a redshift of $\lambda_{cryst} - \lambda_{amorph}$ = 168 pm, while the higher absorption coefficient increases the losses α in the RR (thus decreasing τ and the Q factor). As expected, the transmission coefficient t, which only depends on the coupling efficiency between the waveguide and the RR, remains the same in all cases. Finally, labelling the amorphous phase as the 'off' state and the crystalline one as the 'on' state, the combination of both effects produces a modulation of 12.36 dB at $\lambda = 1550.384$ nm. In this case, the insertion loss in the 'on' state is -2.5 dB.

3.3.2 Time response of the RR

All of the aforementioned measurements were static, but it is also interesting to investigate the time response of the device. For this purpose, the ASE source was replaced by a tunable laser (HP 8168F) and the OSA by a fast photodiode (ThorLabs PDA8GS, $<$1 ns rise time). In this way, the laser was tuned at the respective λ_{res} of the amorphous/crystalline state

and the response of the device during one crystallization/reamorphization pulse was monitored by an oscilloscope (see Figure 3.8).

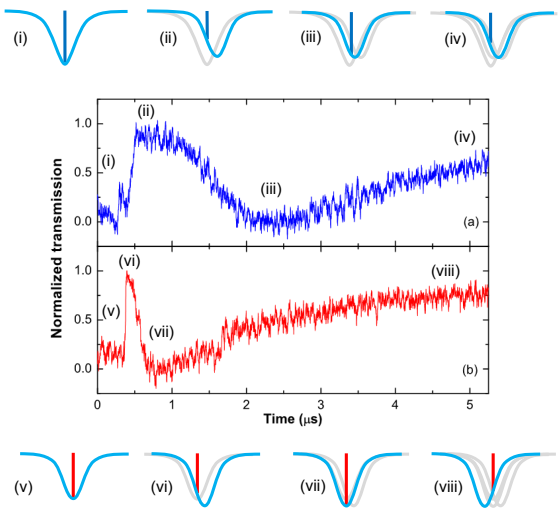

Figure 3.8: Time response of the device during (a) a crystallization pulse ($\lambda_{res} = 1550.384$ nm) and (b) a reamorphization pulse ($\lambda_{res} = 1550.552$ nm). Increasing values in the graph indicate higher transmission at that wavelength.

The dynamics of this response can be understood if one considers the light induced phase transition of the GST film as well as thermal effects in the Si RR following light absorption in the GST. Note that in this experiment, the former can be generated by the pump beam while the latter by both the pump and probe laser. Let us first consider the RR without GST. In this case the above effects are not present (absence of PCM). In addition, the thermo-optic effect due to only Si absorption is experimentally confirmed to be negligible. For the RR with GST, when the switching laser pulse reaches and is absorbed by the amorphous GST, it heats it up, thus starting to induce crystallization, and at the same time causing a redshift of the resonance (observed as an increase in transmission in Figure 3.8a(ii)). As a consequence of this redshift, the resonating optical power of the probe in the resonator is reduced, as well as the heating

due to its absorption in the GST. Therefore, a blue-shift of the resonance occurs, causing a drop in transmission (Figure 3.8a(iii)). This blue-shift once again increases the optical power resonating inside and therefore a new redshift occurs, until, after approximately 5 μs, all the induced effects have reached a steady state condition (Figure 3.8a(iv)). When the initial phase is crystalline the dynamics are similar except that they are generated with a shorter pump pulse (20 ns), and that the final resonant wavelength is shorter than the probe one (Figure 3.8b(v)-(viii)).

3.4 Conclusions

In this chapter, we have shown that the optical contrast of GST thin films can be used to reversibly tune the resonances in a Si RR between two well-defined states. Using this effect, which is triggered by means of optical pulses from an IR laser diode, we have achieved an optical switch with an on/off ratio higher than 12 dB and response times of approximately 5 μs, operating at telecommunication wavelengths. By using heat-sinking structures with high thermal conductivity, the time response of the device could be enhanced and limited only by the phase transition times of the GST layer. In addition, optimization of the RR and GST geometries, for instance using larger GST areas to increase the change in n_{eff} upon crystallization, could reduce the insertion loss in the 'on' state well below 1 dB. Moreover, the ability of GST to be electrically switched suggests further improvements in the device, for instance, by triggering these transitions using integrated metal electrodes inside the chip.

Chapter 4

Active Control of Surface Plasmon Polaritons with GST

Photonic devices are promising candidates to implement future communication and information technologies and they have already outperformed their electronic counterparts in terms of speed and losses. One of the main bottlenecks of these technologies is the difficulty in achieving high integration due to the barrier imposed by the diffraction limit [71], limiting their minimum sizes to values on the order of the wavelength of light. Surface plasmon polaritons (SPPs), which exhibit strong confinement of light in the subwavelength regime, have emerged as a promising candidate to solve this drawback of conventional photonic circuits [72–74].

In this chapter it is shown, both theoretically and experimentally, how the unique optical properties of GST can be used to perform nonvolatile control of SPPs propagating in plasmonic waveguides. Grating couplers are used to convert free-space light at λ = 1550 nm into an SPP propagating along a Au/SiO_2 plasmonic waveguide covered with GST films which, upon phase transitions to the crystalline phase, can strongly affect the propagation length of the SPP mode. The effect of the phase transition on the transmitted intensity is investigated for different thicknesses of the GST film and interaction lengths between the GST and the Au/SiO_2 waveguide.

4.1 Surface plasmon polaritons at planar interfaces

SPPs are electromagnetic waves confined to a metal/dielectric interface that originate when incident photons are coupled to the oscillation of surface charges present in the metal. These surface waves travel along the metal/dielectric interface, decaying exponentially inside both surrounding materials, and allow for strong confinement of light. We consider here two isotropic semi-infinite media characterized by complex, frequency-dependent, dielectric functions $\varepsilon_1 = \varepsilon_1' + i\varepsilon_1''$ and $\varepsilon_2 = \varepsilon_2' + i\varepsilon_2''$ separated by a planar interface ($z = 0$), as depicted in Figure 4.1.

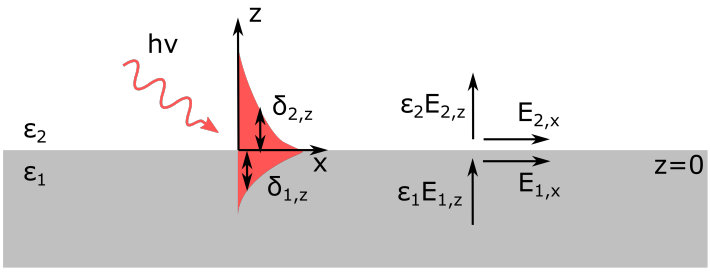

Figure 4.1: Diagram of an SPP propagating along a planar interface between a dielectric and a metal.

In the case of p-polarized surface waves travelling in the positive x direction (SPPs cannot exist for the s-polarized case [75]), one can consider solutions of Maxwell's equations that have the following form:

$$\mathbf{E}_i = \begin{pmatrix} E_{i,x} \\ 0 \\ E_{i,z} \end{pmatrix} e^{ik_{i,z}z} e^{i(k_{i,x}x - wt)}, \quad i = 1, 2 \tag{4.1}$$

Conservation of the momentum parallel to the interface implies $k_{1,x} =$

$k_{2,x} = k_x$, and the wavevector in each media then satisfies the following relation:

$$k_x^2 + k_{i,z}^2 = \varepsilon_i k_0^2, \quad i = 1, 2 \tag{4.2}$$

Applying Gauss's law ($\nabla \cdot \mathbf{D} = 0$) together with the continuity of $\mathbf{E}_\parallel$ and $\mathbf{D}_\perp$ at the interface, one obtains the following equations:

$$k_x E_{i,x} + k_{i,z} E_{i,z} = 0, \quad i = 1, 2 \tag{4.3}$$
$$E_{1,x} - E_{2,x} = 0 \tag{4.4}$$
$$\varepsilon_1 E_{1,z} - \varepsilon_2 E_{2,z} = 0 \tag{4.5}$$

In order to have a solution, the determinant of this system of equations must be zero. This defines the SPP condition, given by:

$$\frac{\varepsilon_1}{k_{1,z}} = \frac{\varepsilon_2}{k_{z,2}} \tag{4.6}$$

Combining 4.6 and 4.2, one obtains the dispersion relation of SPPs:

$$k_x = \frac{w}{c}\sqrt{\frac{\varepsilon_1 \varepsilon_2}{\varepsilon_1 + \varepsilon_2}} \tag{4.7}$$
$$k_{i,z} = \frac{w}{c}\sqrt{\frac{\varepsilon_i^2}{\varepsilon_1 + \varepsilon_2}} \quad i = 1, 2 \tag{4.8}$$

In order to obtain a solution that is bound to the interface, $k_{j,z}$ must be imaginary. Assuming that one of the media is a dielectric with negligible losses ($\varepsilon_2'' = 0$) and the other a metal with $|\varepsilon_1''| \ll |\varepsilon_1'|$, this can only be achieved if the denominator in Eq. 4.8 is negative, i.e. $\varepsilon_1 + \varepsilon_2 < 0$. Using this approximation, the 1/e decay lengths in the x and z directions are then given by:

$$\Lambda_{SPP} = \frac{c}{w}\sqrt{\frac{\varepsilon_1' + \varepsilon_2'}{\varepsilon_1'\varepsilon_2'}} \tag{4.9}$$

$$\delta_{1,z} = \frac{c}{w}\sqrt{\frac{\varepsilon_1' + \varepsilon_2'}{\varepsilon_1'^2}}\left(1 + i\frac{\varepsilon_1''}{2\varepsilon_1'}\right)^{-1} \tag{4.10}$$

$$\delta_{2,z} = \frac{c}{w}\sqrt{\frac{\varepsilon_1' + \varepsilon_2'}{\varepsilon_2'^2}}\left(1 - i\frac{\varepsilon_1''}{2(\varepsilon_1' + \varepsilon_2')}\right)^{-1} \tag{4.11}$$

4.2 Design and simulation of plasmonic waveguides with GST

Before the fabrication of the plasmonic waveguides, it was necessary to find the appropriate thicknesses of each layer and investigate the effect of the GST phase transition in the propagation of SPPs in order to optimize the contrast in the transmitted intensity. Figure 4.2 shows the cross-section of the simulated structures. The structure contains a Ti layer between the Au waveguide and the substrate in order to improve adhesion of Au as well as to avoid the presence of an additional SPP mode in the Au/SiO_2 interface. The top PMMA layer is used to protect the whole device.

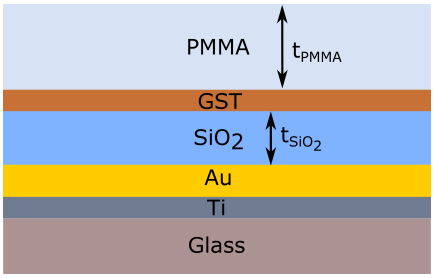

Figure 4.2: Cross section (not to scale) of the simulated SPP waveguides.

The electromagnetic eigenmodes of this system were numerically solved

using OpenMaxWell [76]. The simulations were performed at λ = 1550 nm. The thicknesses of the Ti, Au and GST layers were kept fixed at 30 nm, 60 nm and 30 nm, respectively, during the simulations. The values of the dielectric function at λ = 1550 nm for each material are given in Table 4.1.

Material	$\varepsilon' + i\varepsilon''$
GST_{am}	22.05 + i1.88
GST_{crys}	45 + i8
SiO_2	2.15
Au	-121.38 + i12.06
Ti	-7.10+ i33.45
PMMA	2.19

Table 4.1: Dielectric function at λ = 1550 nm of the different materials used to simulate the SPP waveguide structure.

The optimized structure consists of a SiO_2 layer of t_{SiO_2} = 156 nm and a PMMA layer of t_{PMMA} = 2.1 μm. The reason for using these values is explained below. The structure supports 2 SPP modes, corresponding to the Au/SiO_2 and Ti/substrate interfaces, as well as three waveguided modes due to the presence of the PMMA layer. Each of these modes has a characteristic spatial profile in the y-z plane, as shown in Figure 4.3, and a different propagation constant in the longitudinal direction $k_i = k_i' + ik_i''$. The normalized values of k_i, $n_i' = k_i'/k$ and $n_i'' = k_i''/k$, where $k = \frac{2\pi}{\lambda}$, are given in Table 4.2.

In a real device, a grating coupler is necessary to couple free-space light in and out of the waveguide. To do that, one needs to match the incoming momentum parallel to the interface, $k_x = k \sin\theta$, where θ is the incidence angle, to that of a particular mode with longitudinal wavevector k_i'. This is achieved by choosing an appropriate grating period G to compensate the momentum mismatch via the relation $k_i' = k \sin\theta + i\frac{2\pi}{G}$, where i is an integer [77, 78]. Setting G = 1 μm allows one to efficiently couple the incident radiation to the two SPP modes that have similar values of k_i', while at the same time avoiding efficient coupling into the waveguided

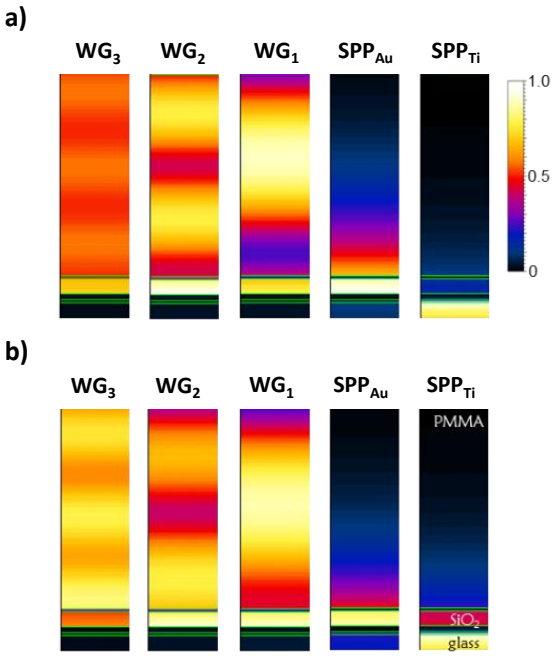

Figure 4.3: Normalized intensity profile of the eigenmodes supported by the structure sketched in Figure 4.2 for t_{SiO_2} = 156 nm and t_{PMMA} = 2.1 μm, with GST in the amorphous (a)) and crystalline (b)) phases.

Mode	$n'_{i,am} + in''_{i,am}$	$n'_{i,crys} + in''_{i,crys}$
SPP_{Au}	1.5332 + i0.0038	1.5477 + i0.0202
SPP_{Ti}	1.5541 + i0.0397	1.5534 + i0.0418
WG_1	1.4251 + i0.0016	1.4375 + i0.0125
WG_2	1.2975 + i0.0039	1.3460 + i0.0321
WG_3	1.1060 + i0.0072	1.1772 + i0.0298

Table 4.2: Propagation constants of the different modes present in the SPP waveguide structure for GST_{am} and GST_{crys}.

modes that have smaller values of k_i'. Moreover, as the value of k_i' for the SPP modes is really similar in the amorphous and crystalline cases, the coupling efficiency will be the same in both states of the device, thus decoupling this effect in the measurements. Also there is a strong change in k_i'' for the SPP$_{Au}$ mode due to a phase transition, which is necessary to achieve high contrast in the transmitted intensity. Finally, the high value of k_i'' for the SPP$_{Ti}$ mode in both cases confirms the usefulness of the additional Ti layer to avoid the appearance of an SPP mode in the Au/substrate interface.

4.2.1 Influence of the PMMA layer

In order to investigate the influence of the PMMA layer on the performance of the device, we simulated the same structure with a fixed value of t_{SiO_2} = 156 nm and varying values of t$_{PMMA}$. The decay length Λ_{SPP} of the SPP$_{Au}$ mode as a function of t$_{PMMA}$ for each GST phase is shown in Figure 4.4.

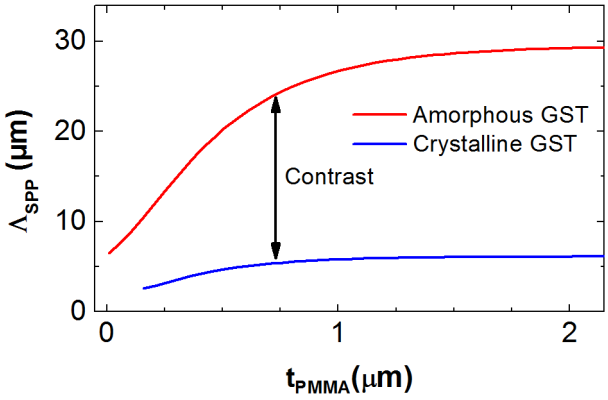

Figure 4.4: Decay length of the SPP$_{Au}$ mode as a function of PMMA thickness for the crystalline and amorphous phases of GST.

Figure 4.4 shows that the contrast is larger for thicker PMMA layers, and its value saturates for values of t_{PMMA} larger than 1.5 μm. However, the thicker the PMMA layer, the larger the number of waveguided modes in the system, thus we decided to work with a value of $t_{PMMA} \approx 2$ μm.

4.2.2 Influence of the SiO_2 layer

Another important parameter that defines the performance of the SPP waveguides is the thickness of the SiO_2 layer, because it determines the interaction between the SPP_{Au} mode and the GST layer. Figure 4.5 shows the evolution of the longitudinal propagation constant and the decay lengths of the different modes as a function of t_{SiO_2}.

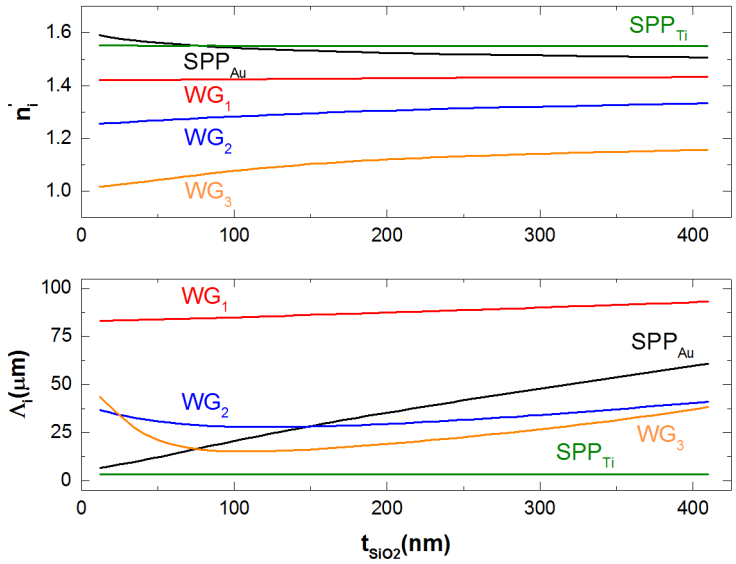

Figure 4.5: Normalized propagation constants (n_i') and propagation lengths (Λ_i) of the different eigenmodes as a function of the SiO_2 layer thickness with GST in the amorphous phase.

Figure 4.5 shows that the thickness of the SiO_2 layer mostly influences the propagation length of SPP_{Au}, while only slightly influencing the value

of n_i' of the different modes for thicknesses below 100 nm. For thin SiO_2 layers, the propagation length in the amorphous phase is small and thus there would be no signal at the output grating. On the other hand, if the GST layer is too far away from the Au/SiO_2 interface, the SPP_{Au} mode would not interact with this layer in the crystalline phase and there would be no contrast in the transmitted intensity. Therefore, we chose a value of t_{SiO_2} = 156 nm in order to allow for high contrast without reducing the propagation length in the amorphous phase.

4.3 Propagation length and contrast of the SPP waveguides

In order to measure the effect of GST in the propagation of SPPs, we fabricated devices with the same configuration simulated in the last section. Figure 4.6 shows a schematic of these devices.

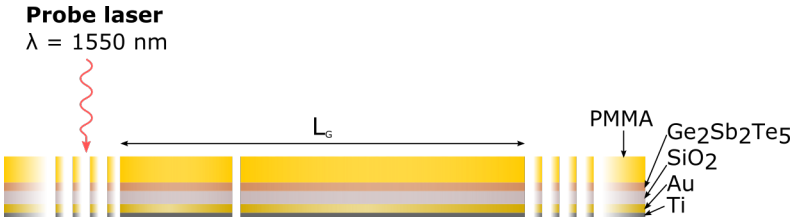

Figure 4.6: Schematic of the device used to probe the propagation length of SPP_{Au}.

The devices consist of two grating couplers designed to couple free space light at λ = 1550 nm in- and out- of the device. The SPP waveguide inbetween them has a length L_G and is fully covered by a 30 nm GST layer. Additionally a groove-like line defect is placed 20 μm away from the input grating in order to normalize the transmitted intensity for different values of L_G.

4.3.1 Device fabrication and experimental set-up

The devices sketched in Figure 4.6 were fabricated by first structuring the gratings and waveguide parts with e-beam lithography, employing a positive tone e-beam resist. After developing the exposed areas, 30 nm thick Ti and 60 nm thick Au films were deposited by thermal evaporation. Then a top layer of 156 nm of SiO_2 was radio frequency (RF) sputtered from a high-purity target in an Ar atmosphere of 0.5 Pa and the 30 nm thick GST films were deposited by RF co-sputtering from stoichiometric targets of GeTe and Sb_2Te_3, using the same conditions given in Table 3.1. Finally, the residual photoresist at the areas unexposed by the electron beam was lifted-off and the whole device was covered with a 2.1 μm layer of PMMA.

The experimental set-up consisted of a fiber-coupled LD with a center wavelength of λ = 1550 nm. The output of the laser was then collimated and converted into linearly polarized light with an LP, before being focused on the sample using a 20x objective. Alignment of the beam with the input grating was achieved by placing the sample on top of an X-Y stage with a rectangular hole in the middle to allow light transmission. Finally, the transmitted light was focused using a 50x objective and imaged in an InGaAs camera.

4.3.2 Experimental results

Measurements of the transmitted intensity were performed for different values of L_G, obtaining in each case an intensity image in the InGaAs camera, as shown in Figure 4.7 for three different values of L_G.

The bright spots on the left correspond to light scattered at the input grating. The scattered intensity at the output grating on the right is then measured and divided by the intensity scattered at the groove-like defect (labelled A in Figure 4.7a) in order to obtain a normalized intensity I_N for each device. The logarithm of I_N is plotted in Figure 4.8 as a function of L_G both for amorphous and crystalline GST. The phase transition in this case was achieved by heating the device on a hot plate at 200 ^{o}C for

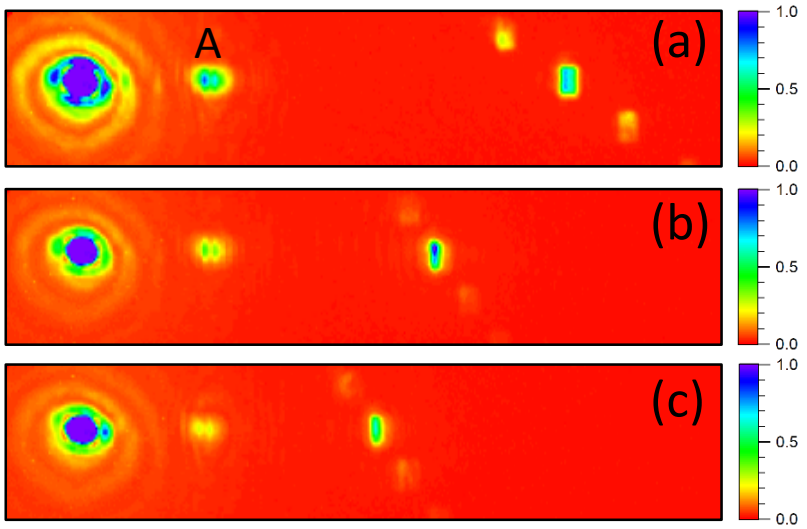

Figure 4.7: Intensity images of the SPP waveguides obtained using the InGaAs camera for three different values of L_G of 160 (a)), 100 (b)), and 80 (c)) μm.

1 h. Then the devices were measured again in order to obtain I_N for the crystalline case.

As shown in Figure 4.8 the intensity along the waveguide decays exponentially in both cases. In the case of crystalline GST, the decay is stronger due to the increased absorption in the GST layer. For values of $L_G > 80$ μm, the losses were too high and no transmitted intensity could be measured and for these values the modulation reaches 100 %. Using this scheme, one can obtain any desired modulation just by choosing an appropriate length of the device.

4.4 Nonvolatile plasmonic switch

Although the devices presented in the last section exhibit strong contrast, they require large areas of GST and long crystallization times. For a real device, one would need to control the phase transition using single laser pulses that crystallize small GST areas while still keeping a reasonable

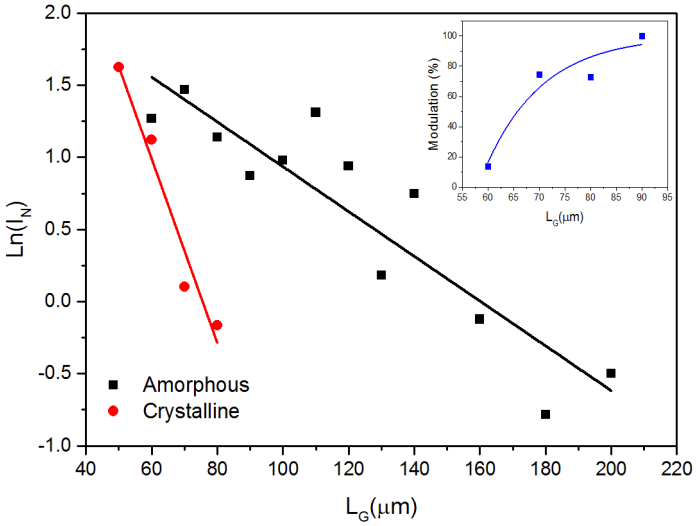

Figure 4.8: Logarithm of the normalized intensity as a function of L_G for amorphous and crystalline GST. Inset: Modulation of the output intensity due to an amorphous to crystalline phase transition.

amount of contrast at the output. In this section, we introduce a nonvolatile plasmonic switch that performs this functionality. The device, sketched in Figure 4.9, is a modification of the one presented above.

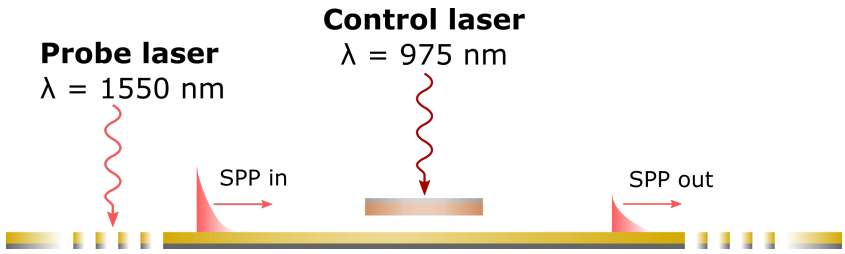

Figure 4.9: Schematic of the nonvolatile switch. An external laser at λ = 975 nm is used to trigger the phase transition in the GST layer.

In this case, an additional control laser at $\lambda = 975$ nm is used to trigger the phase transition in the GST layer. The GST area is only present in the middle of the waveguide and the films are 80 nm thick. An additional 20 nm thick Si_3N_4 is placed on top of the GST film in order to improve heat confinement and facilitate the phase transition. The devices were fabricated using the same procedure explained above, except for an additional e-beam lithography step. This step is done after the deposition of the Au layer in order to pattern the GST area, and is followed by the deposition of the 20 nm Si_3N_4, following the conditions given in Table 3.1, before covering the device with the PMMA layer. A microscope image of the device is shown in Figure 4.10.

The nonvolatile switch consists of two grating couplers separated by a 2 μm wide Au waveguide. The SPP waveguide length is 25 μm, which is smaller than the SPP propagation length for Au embedded in a dielectric slab ($\Lambda_{SPP} \approx 75$ μm at λ = 1550 nm). The grating couplers were placed on larger Au pads in order to reduce the direct transmission of the incident probe laser and to funnel the SPPs to the narrow SPP waveguide [79, 80]. As the real parts of the SPP propagation constants are similar to the case where the GST covers the whole device, the grating periodicity was kept fixed at G = 1 μm.

The principle of operation is as follows: A GST strip of width w is

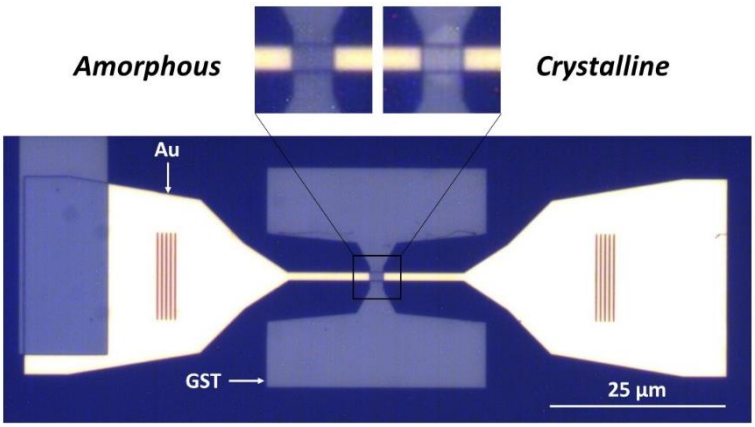

Figure 4.10: Optical microscope image of the nonvolatile plasmonic switch.

placed on top of the SPP waveguide and separated by a 156 nm SiO_2 layer in order to interact with the SPP. As mentioned previously, the thickness of the SiO_2 layer is chosen to obtain a strong mode overlap with the GST layer without sacrificing the transmitted intensity in the amorphous case. The phase transition was triggered with a control laser focused on the GST area down to a spot size of 4 μm, using the same 20x objective as the probe laser. The spot size allowed crystallization with a single pulse of all the region where the GST and the waveguide overlap, for values of $w <$ 4 μm. Single crystallization pulses (t_p^c = 300 ns, t_r^c = 80 ns) with a power of 23 mW were enough to increase the temperature inside the GST layer above T_{crys} and a polycrystalline region was obtained, corresponding to the bright area in the inset of Figure 4.10. The reamorphization process was not possible to achieve in this device, because this transition is much more difficult to trigger in films with this thickness. In this case one would need much higher temperatures to melt the material and high cooling rates in order to quench the liquid state, and this would require the use of a different thermal design with a heat-sinking structure in order to rapidly cool the molten state.

The transmitted light at λ = 1550 nm before and after crystallization

is shown in Figure 4.11 a) and b), respectively, for a waveguide with a GST strip of $w = 5$ μm.

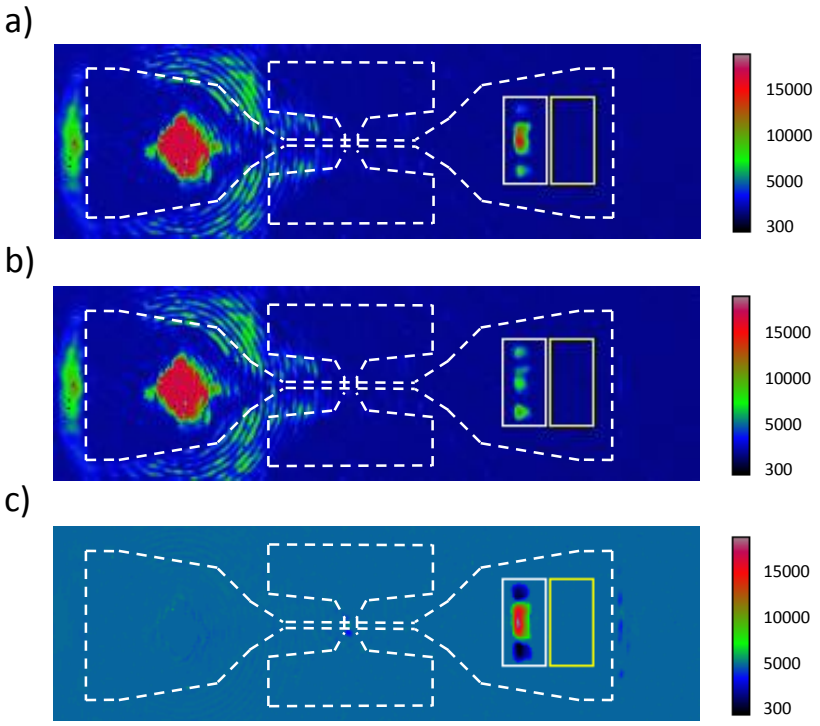

Figure 4.11: Intensity images of the transmitted light as seen by the imaging camera for amorphous a), and crystalline b), GST. The dashed lines are an outline of the actual device. The intense spot on the left side corresponds to the focus placed on the in-coupling grating. The intensity at the output grating changes strongly upon a phase transition, leading to a strong differential signal c).

After irradiating the GST, the transmitted signal is strongly reduced, as shown in Figure 4.11 b). In order to quantify the contrast due to the phase transition, we integrated the intensity in the rectangular area on top of the output grating, as indicated by the white rectangle, to obtain the values I^a and I^{crys}. These values needed to be corrected by measuring the thermal and readout noise in the vicinity of the grating. These were

obtained by integrating the intensity inside the yellow rectangle to get the values I_{bg}^{a} and I_{bg}^{crys}. Assuming the insertion loss is the same in both the amorphous and crystalline cases, these values can be used to calculate the contrast of the device, given by:

$$C = \left| \frac{(I^{crys} - I_{bg}^{crys}) - (I^{a} - I_{bg}^{a})}{I^{a} - I_{bg}^{a}} \right| \tag{4.12}$$

The strong SPP contrast can be visualized by taking the intensity difference of the camera images, as shown in Figure 4.11 c). Most of the image pixels nearly cancel and a large difference in the intensity is found only at the output grating. In this case, the contrast calculated using Eq. 4.12 is C = 31.8 %. The experimental error, obtained by calculating the difference in the average intensity of the same image taken at two different times, is smaller than 0.5 % in both cases.

It is also important to estimate the energy required to switch the device. The fluence of the control laser was 1.8 W·m^{-2} and the total energy required to switch the device was 6.9 nJ, comparable to other plasmonic switches [81].

As the contrast is based on the fact that the SPPs have significantly different absorption lengths for the two GST phases, it is interesting to evaluate the influence of the GST area on the performance of the device. To this end, the same experiment was repeated using different GST widths (w = 0.5, 1, 1.5, 2, 2.5, and 3 μm) for a fixed Au waveguide width of 2 μm. For each value of w, the measurement was performed on three different devices. The results are shown in Figure 4.12. The experimental points indicate the mean value of the contrast, and the error bars, its standard deviation. For the wide GST strip (w = 5 μm) full crystallization could not be achieved because the spot size of the laser was smaller than the overlap region, and thus the experimental contrast is smaller than the simulated one. As expected, the contrast increases for wider GST regions due to a longer interaction length, which leads to larger absorption of the light propagating along the waveguide.

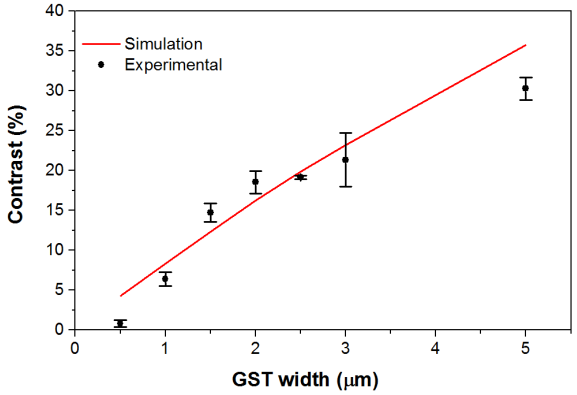

Figure 4.12: Measured and simulated contrast of the SPP waveguides as a function of the width w of the GST area.

4.5 Conclusions

In this chapter, we have demonstrated inhibition of SPP propagation in Au/SiO_2 plasmonic waveguides by exploiting the high contrast in the optical properties of GST. The attenuation in the transmitted intensity strongly depends on the interaction length between the Au waveguide and the GST. For devices completely covered with GST this contrast can reach values of 100 %. For integrated devices, where one wants to control the phase transition using single laser pulses, a contrast of approximately 30 % is achieved using only 6.9 nJ of optical energy. These results demonstrate that the combination of SPPs with GST allows the design of non-volatile plasmonic switches with the desired contrast.

Finally, we expect that an improved thermal design could both reduce the crystallization time down to the few ns regime, requiring less energy to switch the device, and allow it to be reversibly switch it between the amorphous and crystalline states.

Chapter 5

Ultrafast and broadband tuning of resonant optical nanostructures

Nanostructured devices containing metallic elements can support plasmons, which can confine and guide light below the diffraction limit. In particular, plasmons have been shown to play an important role in the phenomenon of extraordinary optical transmission (EOT) through periodic arrays of nanoholes (NH) patterned in metallic films. Resonances in the transmitted spectrum have been attributed to resonant interactions between holes mediated by surface plasmons [82], and can be easily explained in terms of geometrical resonances in the periodic lattice [83–85].

One of the main challenges in the design of these plasmonic nanostructures is the precise control of their optical properties. This can be achieved by an appropriate choice of the materials and geometries. However, this approach is static and limited by material inhomogeneities and fabrication tolerances. Due to the high sensitivity of surface plasmons to local variations in the refractive index, other approaches have been based on the use of active materials whose refractive index can be changed using an external stimulus, for instance using quantum dots [86] or liquid crystals [87].

In this chapter, we introduce different designs combining thin films of GST with arrays of NHs patterned in Au films and demonstrate their capability to obtain broadband and ultrafast tuning of transmission resonances both in the visible and near-infrared (NIR) spectral regions. Specifically the purpose of this chapter is twofold. On the one hand, we show large wavelength and amplitude tuning of the EOT resonances based on a GST phase transition. This effect is explored for 3 different geometries, obtaining resonance wavelength shifts as large as 385 nm, an order of magnitude higher than previously reported [87]. On the other hand, we demonstrate ultrafast tuning of the EOT resonances in the ps regime based on changes in the resonant bond polarizability of GST [88]. This is achieved without the need of a phase transition, thus making the process reversible and overcoming the limit imposed by the cycleability of GST.

5.1 Au NH array with GST inside the holes

The first device consists of a hexagonal NH array patterned on top of a 40 nm thick Au film. A 20 nm GST film is deposited both on top of the Au film and inside the NH, as sketched in Figure 5.1 a). The hole diameter (d) is 250 nm and the period of the hexagonal lattice (a) is 470 nm.

5.1.1 Device fabrication

The device was fabricated on top of a fused SiO_2 substrate using colloidal lithography. A 50 μL solution of polystyrene (PS) beads (10 % concentration), with a nominal diameter of 470 nm, was mixed in ethanol in a 1:1 volume ratio and placed in an ultrasonic bath for 30 minutes. A laminar flow of the prepared solution was then created on the surface of distilled water using a curved pipette with its tip placed just above the water surface. The water was contained in a small box where the SiO_2 substrate had been previously immersed. After a few minutes, the water surface was fully covered by a polycrystalline monolayer of hexagonally packed PS beads and, upon removal of the distilled water, the monolayer was de-

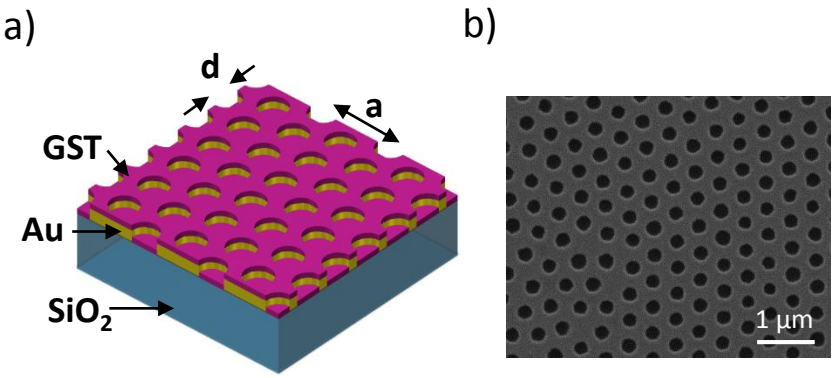

Figure 5.1: Schematic of a NH array with GST inside the holes

posited on top of the substrate. Then the PS beads were shrunked down to a diameter of 250 nm by reactive ion etching (RIE) using O_2 plasma for 4'15" at 100 W. A 5 nm Ti adhesion layer and a 40 nm Au layer were then thermally evaporated on top. This was followed by the removal of the PS beads with a scotch tape before depositing the 20 nm GST layer by RF co-sputtering using the conditions given in Table 3.1. An SEM image of the fabricated device is shown in Figure 5.1 b).

5.1.2 Transmission measurements

Transmission measurements were performed at normal incidence for wavelengths between 300 and 2400 nm in a commercial spectrophotometer using a wavelength step of 5 nm and a rectangular beam of 3×8 mm^2. Figure 5.2 a) shows the transmission spectrum of the device both for amorphous (blue curve) and crystalline (green curve) GST. The transmission of a Au NH array without GST is also shown as a reference (orange curve). A peak in transmission associated with EOT can be clearly seen in all

cases.

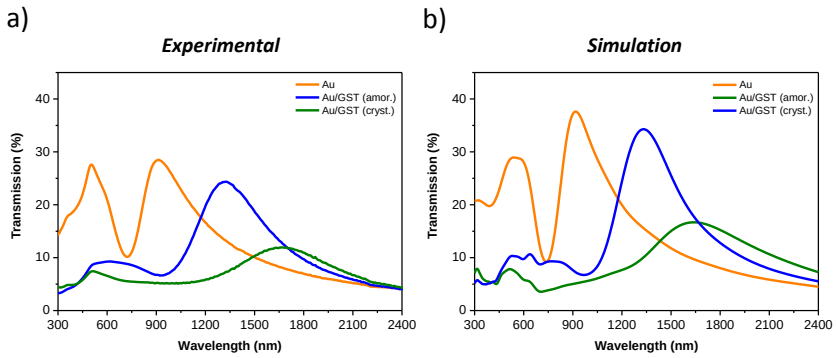

Figure 5.2: Experimental and simulated transmission spectrum of a bare NH array (orange curve) and a NH array with amorphous (blue curve) and crystalline (green curve) GST.

The transition between amorphous and crystalline GST was triggered by heating the sample on a hot plate at 200 °C. Heating for about 1 minute was sufficient to completely crystallize the film, and no further changes in the spectrum were observed after subsequent thermal treatments. After crystallization, the initial resonance wavelength λ_{res}^{a} = 1330 nm is redshifted by 385 nm (λ_{res}^{c} = 1715 nm), and the peak transmission is decreased by >60 % due to the change in the optical constants of GST. This was confirmed by FDTD simulations of the same structure, as shown in Figure 5.2 b). The simulated electric field distribution on- and off- resonance when the GST is in the crystalline phase is shown in Figure 5.3. The electric field distribution supports the idea that the GST modifies the SPPs in the NH array.

5.1.3 Ultrafast response of the NH array

This device was also used to investigate changes in EOT resonances via optical pumping associated with the ultrafast and reversible dynamics of the resonant bond polarizability. It is known that for pump fluences below

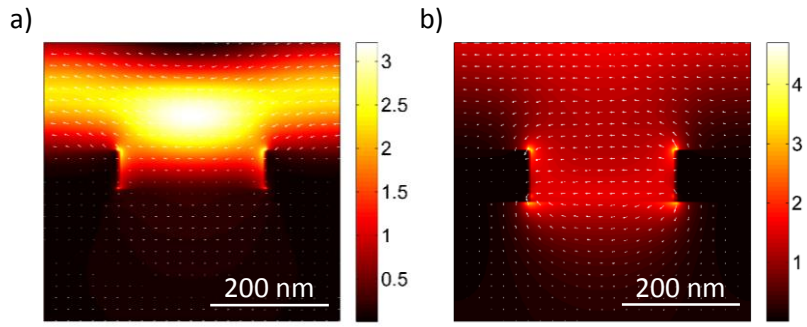

Figure 5.3: Simulated electric field distribution off- (λ = 1200 nm, a)) and on-resonance (λ = 1715 nm, b)) when the GST is in the crystalline phase.

the threshold required to reamorphize, GST is capable of transiently and rapidly acquiring values of the dielectric function close to those of the amorphous state without completing the phase-transition [88]. Moreover this effect takes place in the ultrafast timescale (ps) and is reversible.

For this purpose, a pump-probe experiment was performed. Starting with crystalline GST, 35 fs pump pulses at 800 nm with a fluence of 5 mJ·cm^{-2} were used to pump the sample with a repetition rate of 80 Hz. The reduced repetition rate was needed in order to avoid cumulative heating of the sample, which could lead to reamorphization of the GST film. Then, infrared pulses with a duration of 60 fs, generated in an optical parametric amplifier, measured the transmission of the sample at different time delays and for wavelengths between 1150 and 2150 nm in 100 nm spectral steps. The transmitted light was collected as a function of probe delay using a photodiode and lock-in detection. The time-resolved evolution of the transmitted spectrum during the initial 3 ps is shown in Figure 5.4.

In order to verify that this response is due to the GST, we also performed the same pump-probe experiment using a bare Au NH array, con-

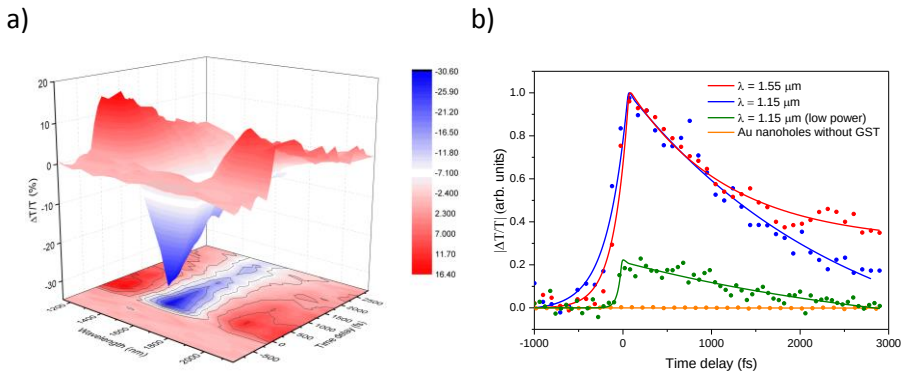

Figure 5.4: a) Time response of the NH array between λ = 1150 - 2100 nm during the initial 3 ps. b) Normalized time response at λ = 1550 nm and λ = 1150 nm using a pump fluence of 5 mJ·cm^{-2}. For lower pump fluences (F = 1.5 mJ·cm^{-2}, green circles), the sample shows the same behavior with a smaller modulation. The time response of a bare Au NH array is also shown at λ = 1150 nm (orange circles).

firming that pumping the bare Au sample does not modify the transmission, as shown in Figure 5.4 b) (orange circles). At telecom wavelengths the sample containing GST shows a decrease in transmission due to the ultrafast change in the dielectric function of GST. The modulation is fast, reaching a peak value in 100 fs (resolution limited) and recovering after a few ps. Furthermore, the magnitude of the modulation is already > 30 % for modest excitation power.

The origin of this modulation is a transient change in the dielectric function in the ps timescale [88]. It has been shown that in this case the dielectric function achieves values which are close to, but not equal, to those of the stable amorphous phase. Thus a new resonant feature arises in this regime which does not need to be the same as in the static case. This can be clearly seen, for instance, at λ = 1550 nm, where the change is positive in the static case and negative in the ultrafast regime. One would need a complete characterization of the dielectric function of the

sample in the IR region probed here in order to give a definitive statement about the origin of the positive signals appearing at other wavelengths. Most likely, these signals arise from a combination of the change in the dielectric function, a transient increase in carriers induced by the pump pulse, phonon contributions and the effects of nanostructuring [89].

5.2 Au NH array without GST in the holes

After investigation of the first device, a second was designed and fabricated, consisting of a Au NH array with the same geometry but without GST inside the holes. The fabrication procedure was identical except that in this case the PS beads were removed after the deposition of the GST layer. The experimental transmission spectrum for amorphous and crystalline GST is shown in Figure 5.5 a).

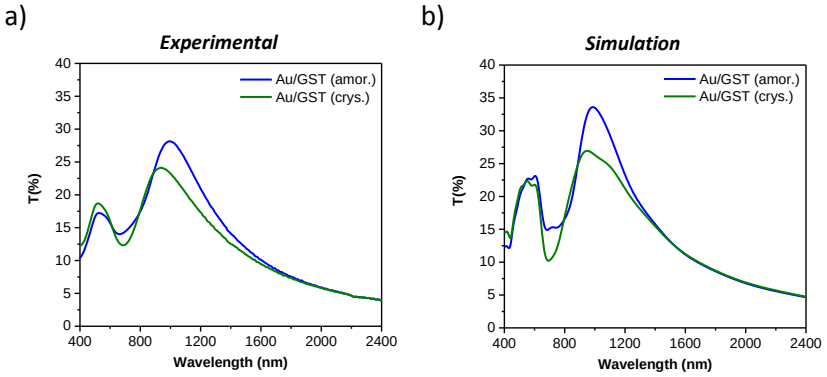

Figure 5.5: Experimental and simulated transmission spectrum of a NH array with amorphous (blue curve) and crystalline (green curve) GST when the GST is only present on top of the Au surface.

In this sample, the amorphous to crystalline phase transition, which was again triggered again by heating the sample on a hot plate at 200 °C for 1 minute, produces a resonance wavelength blueshift of 35 nm. The transmission of the NH array slightly decreases from 28 % to 24 %. These

changes are in agreement with FDTD simulations, as shown in Figure 5.5 b).

Moreover, this sample was also used to demonstrate electrical tuning of the optical transmission by electrically triggering a phase transition in the GST layer. Using two lateral 40 nm thick Au films as planar contact electrodes and applying a DC current (V_c = 3.5 V; I_c = 1.5 A), the GST layer crystallized in approximately 20 s due to Joule heating of the Au film underneath the GST, which increased its temperature above the crystallization temperature. Subsequent application of the same DC current did not change the transmission anymore, indicating that the GST layer had been completely crystallized. The effect of this electrically triggered phase transition on the transmitted spectrum is shown in Figure 5.6. The measurements confirmed that this effect is similar to the previous case, producing a blue shift of 35 nm and a decrease in the transmission from 33 % to 26 %.

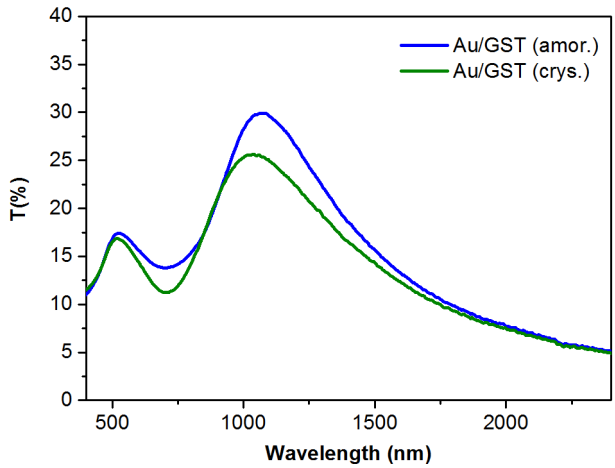

Figure 5.6: Evolution of the NH array spectrum when the phase transition is electrically triggered.

5.3 Au NH array in a Si_3N_4 membrane

For certain applications, it is desirable to have narrower resonances than those of the two devices presented before, whose values are on the order of hundreds of nm, mainly due to the polycrystalline structure of the PS beads used to fabricate them. For this purpose, a third device was investigated, consisting of a periodic NH array perforated in a 100 nm free-standing Si_3N_4 membrane covered with a 125 nm thick Au film and a 10 nm GST film, as sketched in Figure 5.7.

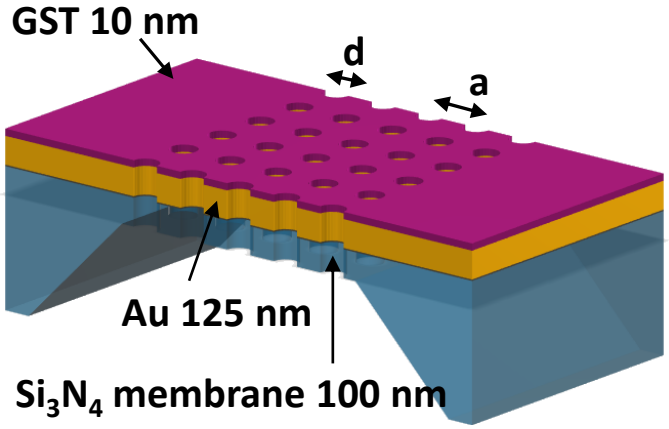

Figure 5.7: Schematic of a NH array on a Si_3N_4 membrane.

The device was fabricated at EPFL using a combination of deep ultraviolet lithography and RIE, as described in ref. [87]. This method was used to pattern a square lattice of NHs with a period of a = 600 nm and a diameter of d = 200 nm, which displays much sharper resonances in the transmission spectrum. Optical characterization of this sample was performed via spectroscopic measurements using an unpolarized broadband white light source. Transmitted light from the device was collected by a high-magnification objective lens (100x Nikon objective lens with NA of 0.6 embedded in a Nikon Eclipse-Ti microscope) coupled with an optical fiber and recorded with a Maya 2000Pro spectrometer. The transmission

measurements are shown in Figure 5.8.

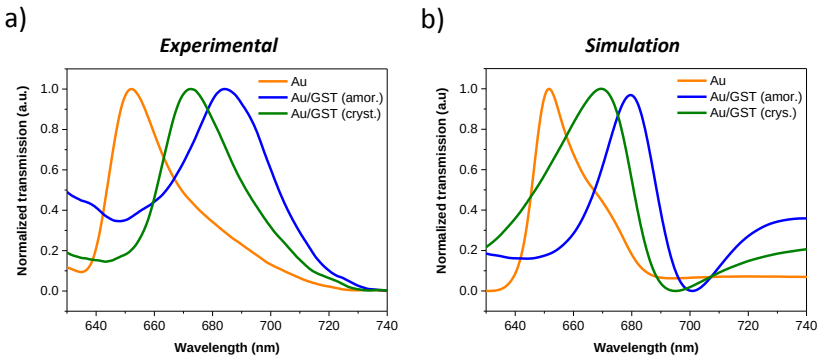

Figure 5.8: Experimental and simulated normalized transmission of the NH array suspended on a Si_3N_4 membrane both without (orange curve) GST and with GST in the amorphous (blue curve) and crystalline (green curve) phases.

In this case, the wavelength range and the resonance bandwidths are respectively about 20 and 10 times smaller than those of the NH array with GST inside the holes. Crystallization of this sample induces a blue shift of 13 nm in the resonance wavelength, due to the smaller thickness of the GST layer (10 nm). Again, the measured values were confirmed by FDTD simulations, as shown in Figure 5.8 b).

5.4 Physical origin of the change in the transmission spectrum

Although FDTD simulations were in good agreement with the experimental values, it is also interesting to investigate the physical origin of the changes in the transmission spectrum, which lie in the large optical contrast of GST. After a phase transition, both its refractive and absorption coefficient increase for wavelengths above 450 nm. Thus, one would expect to see lower transmission and a shift in the resonance wavelength after crystallization.

One can gain further insight into the effect of a GST phase transition on the EOT resonances through a qualitative description of the sample using a semianalytical model that describes the interaction of light with the nanostructured surface [85]. For diameters and periods smaller than the wavelength, light transmission through NH arrays in metallic films can be modelled in terms of equivalent induced electric (p_1, p_2) and magnetic (m_1, m_2) dipoles on each side of the film [85, 90]. For simplicity, assuming perfect electric conductors (PEC), only electric dipoles perpendicular to the film and magnetic dipoles parallel to it can be excited. Moreover, under normal incidence only magnetic dipoles dominate the response [91], whose values are given by:

$$m_1 = \frac{\alpha_1 + (\alpha_1\alpha_2 - \alpha_1'\alpha_2')G_2}{(1-\alpha_1 G_1)(1-\alpha_2 G_2) - \alpha_1'\alpha_2' G_1 G_2} H^{ext} \tag{5.1}$$

$$m_2 = \frac{\alpha_2'}{(1-\alpha_1 G_1)(1-\alpha_2 G_2) - \alpha_1'\alpha_2' G_1 G_2} H^{ext} \tag{5.2}$$

Here, H^{ext} is the external magnetic field at the opening of the holes, including the specularly reflected field from the metal surface; α_1, α_2 and α_1', α_2' are the polarizabilities of the top (α_1, α_1') and bottom (α_2, α_2') magnetic dipoles when the field is propagating in the forward (α_1, α_2) or backward (α_1', α_2') direction. These polarizabilities can be explicitly calculated using a modal expansion method, as shown in [92]. Finally the interaction between dipoles in the upper and lower sides of the film is encoded in the lattice sums G_1 and G_2, respectively, which display characteristic divergences that appear as lattice resonances in the spectra [91]. Knowing these parameters and that the field radiated by a magnetic dipole ($\mathbf{m}_i$) placed at position $\mathbf{r}_i$ is:

$$\mathbf{E}_{i,scat}(\mathbf{r}) = (-ik\mathbf{m}_i \times \nabla)\frac{e^{ik_z|\mathbf{r}-\mathbf{r}_i|}}{|\mathbf{r}-\mathbf{r}_i|} \tag{5.3}$$

one can calculate the far-field transmission coefficient summing up the contributions from all dipoles sitting on the lower side of the film, which leads to:

$$T = \left| \frac{2\pi i k m_2}{A} (1 - r_{23}) \right|^2 \tag{5.4}$$

where A is the area of a unit cell of the NH array and r_{23} is the reflection coefficient at the interface between the Au film and the SiO_2 substrate.

Both the magnetic polarizabilities and lattice sums depend on the material and geometrical parameters and are sensitive to the presence and optical properties of GST. The difference in the magnitude and direction of the shifts between the first device (redshift) and the other two (blueshift) is, therefore due to the presence of GST inside the holes. The position of the resonance wavelength is given by the combined effect of the change in the polarizability of the holes and the change in the interaction between them. In the first device, the polarizability increases when the GST crystallizes, thus redshifting the resonance position, and this effect surpasses the small blueshift due to the change in the interaction terms. This is note the case for the other two devices, where the combined effect leads to a blueshift due to a much smaller change in the polarizability that does not compensate the blueshift due to the change in the interaction terms.

5.5 Conclusions

In this chapter, we have demonstrated optical tuning of resonant NH arrays patterned in Au films using GST. The high contrast in the optical properties of GST enables thermal tuning of the resonant response with spectral shifts as large as 385 nm and modulation depths $> 60\%$, larger than those previously reported for other designs. Additionally, in one of the samples we have shown that electrical tuning can also be achieved using Au electrodes to crystallize the GST, obtaining results similar to the thermal case. Moreover, for the sample exhibiting the largest shift and modulation, our work shows that the tuning can also be optically induced without the GST undergoing any phase transition, thus extending the device lifetime. The resulting optically induced modulation is still

large (30%) and occurs over an ultrafast timescale in the ps domain. We have also shown that this effect can be exploited in the visible regime by designing a resonant nanostructure with sharper resonances and larger Q-factors using e-beam lithography, opening a way to use them for different applications, such as biosensors [93] or plasmonic tuning [94]. With proper scaling, the proposed designs could be extended to the mid-infrared, as GST also exhibits large changes in the optical properties in this regime. Finally, the low-cost nanofabrication methods used in this work [95, 96] for patterning nanostructures incorporating PCMs hold great potential as the basis to manufacture ultrafast and tunable optical devices operating over a wide spectral range.

Chapter 6

Conclusions and Outlook

Photonic devices are one of the most promising candidates to implement future information and communication technologies. These devices have already surpassed current electronic circuits in terms of speed, but due to the diffraction limit of light, their miniaturization is still the subject of a lot of research. Moreover, as light does not interact with itself, controlling light with light is not as straightforward as controlling electrons. Therefore, proper control of light in integrated devices is one of the major cornerstones for the success of photonic technologies.

To this end, this thesis is devoted to the design and implementation of photonic devices based on PCMs. These compounds have particular features that are not found in other materials used in traditional optical devices. In particular, they exhibit large changes in the optical properties, fast phase transition times and the capability to retain their state without the need for an external stimulus. This last feature is particularly important for nonvolatile photonic applications.

The devices presented in this thesis used GST as the active material that allowed for the control of light. Thus, the first step (Chapter 2) was to find out the conditions required to fabricate GST films in a repeatable way and to characterize their properties. These preliminary results were then used to design the devices introduced in this thesis.

The first device, introduced in Chapter 3, is an optical switch operat-

ing at telecommunication wavelengths. It is based on a silicon RR partially covered with a GST thin film (20 nm) with an area of 3×1.5 μm^2. The parameters needed to crystallize and reamorphize GST thin films, as well as a characterization of the temperature response of the RR, are also investigated in this chapter. The demonstrated device shows reversible operation and allows controlling light transmission with light. High on/off ratios ($\sim$ 12 dB) are achieved after phase transitions, while the time response of the device (5 μm) is mainly limited by the thermal properties of the silicon racetrack resonator.

A plasmonic switch using GST is introduced in Chapter 4. In this device, a GST film is used to inhibit the propagation of SPPs along a Au/SiO_2 interface. Two main configurations are investigated. In the first one, where the device is fully covered with a thin film (20 nm) of GST, 100 % contrast in transmission is demonstrated for sufficiently long waveguides. However, in this scheme the phase transition is triggered using a hot plate, requiring long crystallization times, thus making it impractical for integrated devices. This is solved in the second configuration, which allows for light control of the phase transition using single laser pulses. This is achieved by using smaller ($\sim5\times2$ μm^2) but thicker (80 nm) GST areas placed in the middle of the waveguide. In this case, a maximum contrast of $\sim$ 30 % can be achieved using low switching energies (6.9 nJ) and crystallization times of $\sim$ 300 ns. The main drawback of this configuration is the impossibility to reamorphize the GST layer due to the large thickness.

In a different direction, the last application, explained in Chapter 5, explores the combination of GST and NH arrays, which exhibit resonances in the transmission spectrum, patterned on thin Au films. Upon an amorphous to crystalline phase transition of a GST film (20 nm) covering the NH array, large wavelengths shifts (385 nm) and modulation depths ($>$ 60 %) of such resonances are demonstrated. The ultrafast response of this device is also investigated using a pump-probe set-up, showing that the resonances can also be reversibly modulated ($>$ 30 %) on the ps timescale without the need for a phase transition. The origin of this fast modulation is an ultrafast change in the electronic polarizability of

GST upon excitation with short pulses (80 fs). As the absence of a phase transition extends the lifetime of the device, this approach is particularly interesting for applications that require a large number of cycles. Another configuration, with GST only on top of the Au film, is also explored, which shows smaller shifts ($\sim$ 35 nm) and can be electrically controlled using Au electrodes. However, these two configurations have broad resonances on the order of hundreds of nm, while for certain applications narrower resonances on the order of few tens of nm are required. Tuning of these narrower resonances is also demonstrated in a third device, fabricated using e-beam lithography on top of a Si_3N_4 membrane, obtaining wavelengths shifts of 13 nm.

Outlook

The feasibility of PCMs for photonic applications has been demonstrated several times over the last few years. Still, there are a few challenges that need to be addressed.

One such challenge is the cycleability of PCMs, which is usually limited to 10^6-10^7 cycles. This is not a problem for nonvolatile and reconfigurable devices, which are not thought to work continuously, but it can be a limitation in other photonic devices, for instance, modulators. One possible solution is the ultrafast excitation of GST presented in Chapter 5, which avoids the cycleability limit due to the absence of phase transitions. Still, the repetition rates are limited to 50-100 Hz, otherwise cumulative heating can cause reamorphization of the sample. Designs with better thermal properties to improve heat extraction are, thus, crucial for future devices. Another issue related to the thermal properties is the capability to reamorphize thick GST films with low laser powers. This would be important for devices like the one presented in Chapter 4, and, again, would require further research on appropriate thermal structures. All these factors, together with improvements in the phase transition times, as well as the search for new PCM compounds with enhanced optical and electrical properties, will be crucial for their use in future photonic devices.

Bibliography

[1] Various, *Phase change materials: Science and applications*, M. Wuttig and S. Raoux, Eds. Springer Verlag, New York, 2008.

[2] S. R. Ovshinsky, "Reversible electrical switching phenomena in disordered structures," *Phys. Rev. Lett.*, vol. 21, pp. 1450–1453, 1968.

[3] M. Wuttig and N. Yamada, "Phase-change materials for rewriteable data storage," *Nature Mater.*, vol. 6, pp. 824–832, 2007.

[4] N. Yamada, E. Ohno, K. Nishiuchi, N. Akahira, and M. Takao, "Rapid-phase transitions of gete-sb2te3 pseudobinary amorphous thin films for an optical disk memory," *J. Appl. Phys.*, vol. 69, no. 5, pp. 2849–2856, 1991.

[5] M. Wuttig, "Phase-change materials: Towards a universal memory?" *Nature Mater.*, vol. 4, no. 4, pp. 265–266, 2005.

[6] M. H. R. Lankhorst, B. W. Ketelaars, and R. A. M. Wolters, "Low-cost and nanoscale non-volatile memory concept for future silicon chips," *Nature Mater.*, vol. 4, pp. 347–352, 2005.

[7] D. Lencer, M. Salinga, B. Grabowski, T. Hickel, J. Neugebauer, and M. Wuttig, "A map for phase-change materials," *Nature Mater.*, vol. 7, no. 12, pp. 972–977, 2008.

[8] D. Loke, T. H. Lee, W. J. Wang, L. P. Shi, R. Zhao, Y. C. Yeo, T. C. Chong, and S. R. Elliott, "Breaking the speed limit of phase-change memory," *Science*, vol. 336(6088), pp. 1556–1569, 2012.

[9] L. Pauling, *The nature of the chemical bond and the structure of molecules and crystals: an introduction to modern structural chemistry*. Cornell university press, 1960, vol. 18.

[10] K. Shportko, S. Kremers, M. Woda, D. Lencer, J. Robertson, and M. Wuttig, "Resonant bonding in crystalline phase-change materials," *Nature Mater.*, vol. 7, pp. 653–658, 2008.

[11] L. Waldecker, R. Bertoni, and R. Ernstorfer, "Compact femtosecond electron diffractometer with 100 kev electron bunches approaching the single-electron pulse duration limit," *J. Appl. Phys.*, vol. 117, no. 4, p. 044903, 2015.

[12] G. Lucovsky and R. White, "Effects of resonance bonding on the properties of crystalline and amorphous semiconductors," *Phys. Rev. B*, vol. 8, no. 2, p. 660, 1973.

[13] T. Nonaka, G. Ohbayashi, Y. Toriumi, Y. Mori, and H. Hashimoto, "Crystal structure of gete and ge 2 sb 2 te 5 meta-stable phase," *Thin Solid Films*, vol. 370, no. 1, pp. 258–261, 2000.

[14] T. Matsunaga and N. Yamada, "A study of highly symmetrical crystal structures, commonly seen in high-speed phase-change materials, using synchrotron radiation," *Jpn. J. Appl. Phys.*, vol. 41(3B), pp. 1674–1678, 2002.

[15] ——, "Crystallographic studies on high-speed phase-change materials used for rewritable optical recording disks," *Jpn. J. Appl. Phys.*, vol. 43, no. 7S, p. 4704, 2004.

[16] A. V. Kolobov, P. Fons, A. I. Frenkel, A. L. Ankudinov, J. Tominaga, and T. Uruga, "Understanding the phase change mechanism of rewritable optical media," *Nature Mater.*, vol. 3, pp. 703–708, 2004.

[17] B. Huang and J. Robertson, "Bonding origin of optical contrast in phase-change memory materials," *Phys. Rev. B*, vol. 81, no. 8, p. 081204, 2010.

[18] J. Orava, A. L. Greer, B. Gholipour, D. W. Hewak, and C. E. Smith, "Characterization of supercooled liquid $ge_2sb_2te_5$ and its crystallization by ultrafast-heating calorimetry," *Nature Mater.*, vol. 11, pp. 279–283, 2012.

[19] G. Zhou, H. J. Borg, J. Rijpers, M. H. Lankhorst, and J. Horikx, "Crystallization behavior of phase change materials: comparison between nucleation-and growth-dominated crystallization," in *Proc. SPIE*, vol. 4090, 2000, pp. 108–115.

[20] G.-F. Zhou and B. A. Jacobs, "High performance media for phase change optical recording," *Jpn. J. Appl. Phys.*, vol. 38, no. 3S, p. 1625, 1999.

[21] G.-F. Zhou, "Materials aspects in phase change optical recording," *Mater. Sci. Eng. A*, vol. 304, pp. 73–80, 2001.

[22] B.-S. Lee, J. R. Abelson, S. G. Bishop, D.-H. Kang, B.-k. Cheong, and K.-B. Kim, "Investigation of the optical and electronic properties of ge2sb2te5 phase change material in its amorphous, cubic, and hexagonal phases," *J. Appl. Phys.*, vol. 97, no. 9, p. 093509, 2005.

[23] H.-K. Lyeo, D. G. Cahill, B.-S. Lee, J. R. Abelson, M.-H. Kwon, K.-B. Kim, S. G. Bishop, and B.-k. Cheong, "Thermal conductivity of phase-change material ge2sb2te5," *Appl. Phys. Lett.*, vol. 89, no. 15, p. 151904, 2006.

[24] A. Pirovano, A. L. Lacaita, A. Benvenuti, F. Pellizzer, and R. Bez, "Electronic switching in phase-change memories," *IEEE Trans. Electron Devices*, vol. 51, no. 3, pp. 452–459, 2004.

[25] D. V. Tsu *et al.*, "Obtaining optical constants of thin gexsbytez films from measurements of reflection and transmission," *J. Vac. Sci. Technol., A*, vol. 17, no. 4, pp. 1854–1860, 1999.

[26] J. González-Hernández, E. López-Cruz, M. Yáñez-Limón, D. Strand, B. Chao, and S. Ovshinsky, "Free carrier absorption in

the ge: Sb: Te system," *Solid State Commun.*, vol. 95, no. 9, pp. 593–596, 1995.

[27] A. Mendoza-Galván and J. González-Hernández, "Drude-like behavior of ge:sb:te alloys in the infrared," *J. Appl. Phys.*, vol. 87(2), pp. 760–765, 2000.

[28] S. Yamanaka, S. Ogawa, I. Morimoto, and Y. Ueshima, "Electronic structures and optical properties of gete and ge 2sb 2te 5," *Jpn. J. Appl. Phys.*, vol. 37, no. 6R, p. 3327, 1998.

[29] I. Friedrich, V. Weidenhof, W. Njoroge, P. Franz, and M. Wutting, "Structural transformations of ge˜ 2sb˜ 2te˜ 5 films studied by electrical resistance measurements," *J. Appl. Phys.*, vol. 87, no. 9; PART 1, pp. 4130–4134, 2000.

[30] T. Kato and K. Tanaka, "Electronic properties of amorphous and crystalline ge2sb2te5 films," *Jpn. J. Appl. Phys.*, vol. 44, no. 10R, p. 7340, 2005.

[31] S. Baily, D. Emin, and H. Li, "Hall mobility of amorphous ge 2 sb 2 te 5," *Solid State Commun.*, vol. 139, no. 4, pp. 161–164, 2006.

[32] D. Ielmini and Y. Zhang, "Evidence for trap-limited transport in the subthreshold conduction regime of chalcogenide glasses," *Appl. Phys. Lett.*, vol. 90, no. 19, p. 192102, 2007.

[33] D. Tanaka, Y. Shoji, M. Kuwahara, X. Wang, K. Kintaka, H. Kawashima, T. Toyosaki, Y. Ikuma, and H. Tsuda, "Ultra-small, self-holding, optical gate switch using ge 2 sb 2 te 5 with a multimode si waveguide," *Opt. Express*, vol. 20, no. 9, pp. 10 283–10 294, 2012.

[34] C. Ríos, P. Hosseini, C. D. Wright, H. Bhaskaran, and W. H. Pernice, "On-chip photonic memory elements employing phase-change materials," *Adv. Mater.*, vol. 26, no. 9, pp. 1372–1377, 2014.

[35] C. D. Wright, Y. Liu, K. I. Kohary, M. M. Aziz, and R. J. Hicken, "Arithmetic and biologically-inspired computing using phase-change materials," *Adv. Mater.*, vol. 23, no. 30, pp. 3408–3413, 2011.

[36] C. D. Wright, P. Hosseini, and J. A. Vázquez Diosdado, "Beyond von-neumann computing with nanoscale phase-change memory devices," *Adv. Funct. Mater.*, vol. 23(18), pp. 2248–2254, 2013.

[37] C. Ríos, M. Stegmaier, P. Hosseini, D. Wang, T. Scherer, C. D. Wright, H. Bhaskaran, and W. H. Pernice, "Integrated all-photonic non-volatile multi-level memory," *Nature Photon.*, vol. 9, no. 11, pp. 725–732, 2015.

[38] T. Cao, C. Wei, R. E. Simpson, L. Zhang, and M. J. Cryan, "Rapid phase transition of a phase-change metamaterial perfect absorber," *Opt. Mater. Express*, vol. 3, no. 8, pp. 1101–1110, 2013.

[39] T. Cao, C.-w. Wei, R. E. Simpson, L. Zhang, and M. J. Cryan, "Broadband polarization-independent perfect absorber using a phase-change metamaterial at visible frequencies," *Sci. Rep.*, vol. 4, p. 3995, 2014.

[40] T. Cao, C. Wei, R. E. Simpson, L. Zhang, and M. J. Cryan, "Fast tuning of fano resonance in metal/phase-change materials/metal metamaterials," *Opt. Mater. Express*, vol. 4, no. 9, pp. 1775–1786, 2014.

[41] W. Dong, Y. Qiu, J. Yang, R. E. Simpson, and T. Cao, "Wideband absorbers in the visible with ultrathin plasmonic-phase change material nanogratings," *J. Phys. Chem. C*, vol. 120, no. 23, pp. 12 713–12 722, 2016. [Online]. Available: http://dx.doi.org/10.1021/acs.jpcc.6b01080

[42] A. Tittl, A.-K. U. Michel, M. Schäferling, X. Yin, B. Gholipour, L. Cui, M. Wuttig, T. Taubner, F. Neubrech, and H. Giessen, "A

switchable mid-infrared plasmonic perfect absorber with multispectral thermal imaging capability," *Adv. Mater.*, vol. 27, no. 31, pp. 4597–4603, 2015.

[43] T. Hira, T. Homma, T. Uchiyama, K. Kuwamura, and T. Saiki, "Switching of localized surface plasmon resonance of gold nanoparticles on a gesbte film mediated by nanoscale phase change and modification of surface morphology," *Appl. Phys. Lett.*, vol. 103, no. 24, p. 241101, 2013.

[44] T. Hira, T. Homma, T. Uchiyama, K. Kuwamura, Y. Kihara, and T. Saiki, "All-optical switching of localized surface plasmon resonance in single gold nanosandwich using gesbte film as an active medium," *Appl. Phys. Lett.*, vol. 106, no. 3, pp. –, 2015. [Online]. Available: http://scitation.aip.org/content/aip/journal/apl/106/3/10.1063/1.4906037

[45] S. Yoo, T. Gwon, T. Eom, S. Kim, and C. S. Hwang, "Multicolor changeable optical coating by adopting multiple layers of ultrathin phase change material film," *ACS Photonics*, vol. 3, no. 7, pp. 1265–1270, 2016.

[46] F. F. Schlich, P. Zalden, A. M. Lindenberg, and R. Spolenak, "Color switching with enhanced optical contrast in ultrathin phase-change materials and semiconductors induced by femtosecond laser pulses," *ACS Photonics*, vol. 2, no. 2, pp. 178–182, 2015.

[47] T. Cao, L. Zhang, R. E. Simpson, and M. J. Cryan, "Mid-infrared tunable polarization-independent perfect absorber using a phase-change metamaterial," *J. Opt. Soc. Am. B*, vol. 30, no. 6, pp. 1580–1585, 2013.

[48] P. Hosseini, C. D. Wright, and H. Bhaskaran, "An optoelectronic framework enabled by low-dimensional phase-change films," *Nature*, vol. 511, no. 7508, pp. 206–211, 2014.

[49] A.-K. U. Michel, D. N. Chigrin, T. W. W. Maß, K. Schönauer, M. Salinga, M. Wuttig, and T. Taubner, "Using low-loss phase-change materials for mid-infrared antenna resonance tuning," *Nano Lett.*, vol. 13, no. 8, pp. 3470–3475, 2013, pMID: 23742151. [Online]. Available: http://dx.doi.org/10.1021/nl4006194

[50] K. Wasa and S. Hayakawa, *Handbook of sputter deposition technology*. Noyes ublications, 1992.

[51] "http://www.ajaint.com/."

[52] Q. F. Xu, B. Schmidt, S. Pradhan, and M. Lipson, "Micrometer-scale silicon electro-optic modulator," *Nature*, vol. 435(7040), pp. 325–327, 2005.

[53] G. T. Reed, G. Mashanovich, F. Y. Gardes, and D. J. Thompson, "Silicon optical modulators," *Nature Photon.*, vol. 4(8), pp. 518–526, 2010.

[54] M. Liu, X. B. Yin, E. Ulin-Avila, B. S. Jeng, T. Zentgraf, L. Ju, F. Wang, and X. Zhang, "A graphene-based broadband optical modulator," *Nature*, vol. 474(7349), pp. 64–67, 2011.

[55] Q. F. Xu and M. Lipson, "All-optical logic based on silicon micro-ring resonators," *Opt. Express*, vol. 15(3), pp. 924–929, 2007.

[56] V. R. Almeida, C. A. Barrios, R. R. Panepucci, and M. Lipson, "All-optical control of light on a silicon chip," *Nature*, vol. 431, no. 7012, pp. 1081–1084, 2004.

[57] S. Xiao, M. H. Khan, H. Shen, and M. Qi, "A highly compact third-order silicon microring add-drop filter with a very large free spectral range, a flat passband and low delay dispersion," *Opt. Express*, vol. 15, pp. 14 765–14 771, 2007.

[58] Q. F. Xu, B. Schmidt, J. Shakya, and M. Lipson, "Cascaded silicon micro-ring modulators for wdm optical interconnection," *Opt. Express*, vol. 14(20), pp. 9431–9435, 2006.

[59] W. Bogaerts, P. De Heyn, T. Van Vaerenbergh, K. De Vos, S. Kumar Selvaraja, T. Claes, P. Dumon, P. Bienstman, D. Van Thourhout, and R. Baets, "Silicon microring resonators," *Laser Phot. Rev.*, vol. 6, no. 1, pp. 47–73, 2012. [Online]. Available: http://dx.doi.org/10.1002/lpor.201100017

[60] W. Welnic, S. Botti, L. Reining, and M. Wuttig, "Origin of the optical contrast in phase-change materials," *Phys. Rev. Lett.*, vol. 98, p. 236403, 2007.

[61] G. Roelkens, D. Vermeulen, F. van Laere, S. Selvaraja, S. Scheerlink, D. Taillaert, W. Bogaerts, P. Dumon, D. van Thourhout, and R. Baets, "Bridging the gap between nanophotonic waveguide circuits and single mode optical fibers using diffractive grating structures," *J. Nanosci. Nanotechnol.*, vol. 10(3), pp. 1551–1562, 2010.

[62] P. Dumon, W. Bogaerts, V. Wiaux, J. Wouters, S. Beckx, J. Van Campenhout, D. Taillaert, B. Luyssaert, P. Bienstman, D. Van Thourhout, and R. Baets, "Low-loss soi photonic wires and ring resonators fabricated with deep uv lithography," *IEEE Phot. Tech. Lett.*, vol. 6(5), pp. 1328–1330, 2004.

[63] R. E. Simpson, M. Krbal, P. Fons, A. V. Kolobov, J. Tominaga, T. Uruga, and H. Tanida, "Toward the ultimate limit of phase change in $ge_2sb_2te_5$," *Nano Lett.*, vol. 10(2), pp. 414–419, 2009.

[64] X. Wei, L. Shi, T. C. Chong, R. Zhao, and H. K. Lee, "Thickness dependent nano-crystallization in $ge_2sb_2te_5$ films and its effect on devices," *Jpn. J. Appl. Phys.*, vol. 46, p. 2211, 2007.

[65] F. G. Della Corte, M. E. Montefusco, L. Moretti, I. Rendina, and G. Cocorullo, "Temperature dependence analysis of the thermo-optic effect in silicon by single and double oscillator models," *J. Appl. Phys.*, vol. 88, no. 12, pp. 7115–7119, 2000.

[66] G. Cocorullo, F. G. Della Corte, I. Rendina, and P. M. Sarro, "Thermo-optic effect exploitation in silicon microstructures," *Sensors and Actuators A: Physical*, vol. 71, no. 1, pp. 19–26, 1998.

[67] Y. Okada and Y. Tokumaru, "Precise determination of lattice parameter and thermal expansion coefficient of silicon between 300 and 1500 k," *J. Appl. Phys.*, vol. 56, no. 2, pp. 314–320, 1984.

[68] J. Teng, P. Dumon, W. Bogaerts, H. B. Zhang, X. G. Jian, X. Y. Han, M. S. Zhao, G. Morthier, and R. Baets, "Athermal silicon-on-insulator ring resonators by overlaying a polymer cladding on narrowed waveguides," *Opt. Express*, vol. 17(17), pp. 14 627–14 633, 2009.

[69] W. N. Ye, J. Michel, and L. C. Kimerling, "Athermal high-index-contrast waveguide design," *IEEE Phot. Tech. Lett.*, vol. 20(11), pp. 885–887, 2008.

[70] R. E. Simpson, P. Fons, A. V. Kolobov, T. Fukaya, M. Krbal, T. Yagi, and J. Tominaga, "Interfacial phase-change memory," *Nature Nanotech.*, vol. 6, pp. 501–505, 2011.

[71] M. Born and E. Wolf, *Principles of optics: electromagnetic theory of propagation, interference and diffraction of light*. Cambridge Univ. Press, 1999.

[72] E. Ozbay, "Plasmonics: Merging photonics and electronics at nanoscale dimensions," *Science*, vol. 311, no. 5758, pp. 189–193, 2006.

[73] D. K. Gramotnev and S. I. Bozhevolnyi, "Plasmonics beyond the diffraction limit," *Nature Photon.*, vol. 4, no. 2, pp. 83–91, 2010.

[74] J. A. Schuller, E. S. Barnard, W. Cai, Y. C. Jun, J. S. White, and M. L. Brongersma, "Plasmonics for extreme light concentration and manipulation," *Nature Mater.*, vol. 9, no. 3, pp. 193–204, 2010.

[75] L. Novotny and B. Hecht, *Principles of nano-optics*. Cambridge university press, 2012.

[76] "OpenMaXwell," http://openmax.ethz.ch.

[77] H. Raether, *Surface plasmons on smooth surfaces*. Springer-Verlag: Berlin, 1988.

[78] J. Renger, S. Grafström, and L. M. Eng, "Direct excitation of surface plasmon polaritons in nanopatterned metal surfaces and thin films," *Phys. Rev. B*, vol. 76, no. 4, p. 045431, 2007.

[79] W. L. Barnes, A. Dereux, and T. W. Ebbesen, "Surface plasmon subwavelength optics," *Nature*, vol. 424, no. 6950, pp. 824–830, 2003.

[80] J. C. Weeber, M. U. González, A. L. Baudrion, and A. Dereux, "Surface plasmon routing along right angle bent metal strips," *Appl. Phys. Lett.*, vol. 87, no. 22, p. 221101, 2005.

[81] R. A. Pala, K. T. Shimizu, N. A. Melosh, and M. L. Brongersma, "A nonvolatile plasmonic switch employing photochromic molecules," *Nano Lett.*, vol. 8, no. 5, pp. 1506–1510, 2008.

[82] W. L. Barnes, W. A. Murray, J. Dintinger, E. Devaux, and T. Ebbesen, "Surface plasmon polaritons and their role in the enhanced transmission of light through periodic arrays of subwavelength holes in a metal film," *Phys. Rev. Lett.*, vol. 92, no. 10, p. 107401, 2004.

[83] U. Fano, "Some theoretical considerations on anomalous diffraction gratings," *Physical Review*, vol. 50, no. 6, p. 573, 1936.

[84] H. Ghaemi, T. Thio, D. e. a. Grupp, T. W. Ebbesen, and H. Lezec, "Surface plasmons enhance optical transmission through subwavelength holes," *Phys. Rev. B*, vol. 58, no. 11, p. 6779, 1998.

[85] F. J. García de Abajo, "Colloquium: Light scattering by particle and hole arrays," *Rev. Mod. Phys.*, vol. 79, pp. 1267–1290, Oct 2007. [Online]. Available: http://link.aps.org/doi/10.1103/RevModPhys.79.1267

[86] D. Pacifici, H. J. Lezec, and H. A. Atwater, "All-optical modulation by plasmonic excitation of cdse quantum dots," *Nature Photon.*, vol. 1, no. 7, pp. 402–406, 2007.

[87] A. E. Cetin, A. Mertiri, M. Huang, S. Erramilli, and H. Altug, "Thermal tuning of surface plasmon polaritons using liquid crystals," *Adv. Opt. Mater.*, vol. 1, no. 12, pp. 915–920, 2013. [Online]. Available: http://dx.doi.org/10.1002/adom.201300303

[88] L. Waldecker, T. A. Miller, M. Rudé, R. Bertoni, J. Osmond, V. Pruneri, R. E. Simpson, R. Ernstorfer, and S. Wall, "Time-domain separation of optical properties from structural transitions in resonantly bonded materials," *Nature Mater.*, vol. 14, no. 10, pp. 991–995, 2015.

[89] T. A. Miller, M. Rudé, V. Pruneri, and S. Wall, "Ultrafast optical response of the amorphous and crystalline states of the phase change material $\mathrm{ge_2sb_2te_5}$," *Phys. Rev. B*, vol. 94, p. 024301, Jul 2016. [Online]. Available: http://link.aps.org/doi/10.1103/PhysRevB.94.024301

[90] F. J. García de Abajo, J. J. Sáenz, I. Campillo, and J. S. Dolado, "Site and lattice resonances in metallic hole arrays," *Opt. Express*, vol. 14, no. 1, pp. 7–18, 2006.

[91] M. Rudé, V. Mkhitaryan, A. E. Cetin, T. A. Miller, A. Carrilero, S. Wall, F. J. G. de Abajo, H. Altug, and V. Pruneri, "Ultrafast and broadband tuning of resonant optical nanostructures using phase-change materials," *Adv. Opt. Mater.*, 2016.

[92] N. Rotenberg, M. Spasenović, T. Krijger, B. Le Feber, F. G. de Abajo, and L. Kuipers, "Plasmon scattering from single subwavelength holes," *Phys. Rev. Lett.*, vol. 108, no. 12, p. 127402, 2012.

[93] S. Lal, S. Link, and N. J. Halas, "Nano-optics from sensing to waveguiding," *Nature Photon.*, vol. 1, no. 11, pp. 641–648, 2007.

[94] M. A. Kats, R. Blanchard, P. Genevet, Z. Yang, M. M. Qazilbash, D. Basov, S. Ramanathan, and F. Capasso, "Thermal tuning of mid-infrared plasmonic antenna arrays using a phase change material," *Opt. Lett.*, vol. 38, no. 3, pp. 368–370, 2013.

[95] P. Patoka and M. Giersig, "Self-assembly of latex particle for the creation of nanostructures with tunable plasmonic properties," *J. Mater. Chem.*, vol. 21, p. 16783, 2011.

[96] S. Aksu, A. E. Cetin, R. Adato, and H. Altug, "Plasmonically enhanced vibrational biospectroscopy using low-cost infrared antenna arrays by nanostencil lithography," *Adv. Opt. Mater.*, vol. 1, no. 11, pp. 798–803, 2013.